1 July 2009 Volume 106 Number 1

Journal of Applied Physics

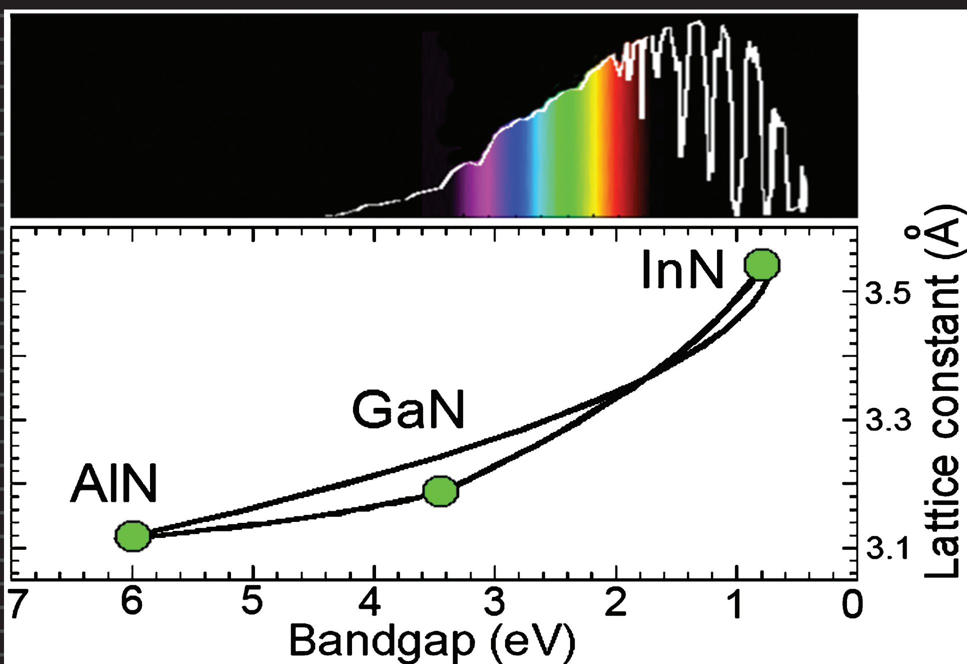

Applied Physics Reviews—Focused Review:
When group-III nitrides go infrared: New properties and perspectives
by J. Wu

American Institute of Physics

APPLIED PHYSICS REVIEWS–FOCUSED REVIEW

When group-III nitrides go infrared: New properties and perspectives

Junqiao Wu[a)]
Department of Materials Science and Engineering, University of California, Berkeley, California 94720, USA and Division of Materials Sciences, Lawrence Berkeley National Laboratory, Berkeley, California 94720, USA

(Received 21 October 2008; accepted 25 February 2009; published online 1 July 2009)

Wide-band-gap GaN and Ga-rich InGaN alloys, with energy gaps covering the blue and near-ultraviolet parts of the electromagnetic spectrum, are one group of the dominant materials for solid state lighting and lasing technologies and consequently, have been studied very well. Much less effort has been devoted to InN and In-rich InGaN alloys. A major breakthrough in 2002, stemming from much improved quality of InN films grown using molecular beam epitaxy, resulted in the bandgap of InN being revised from 1.9 eV to a much narrower value of 0.64 eV. This finding triggered a worldwide research thrust into the area of narrow-band-gap group-III nitrides. The low value of the InN bandgap provides a basis for a consistent description of the electronic structure of InGaN and InAlN alloys with all compositions. It extends the fundamental bandgap of the group III-nitride alloy system over a wider spectral region, ranging from the near infrared at ~1.9 μm (0.64 eV for InN) to the ultraviolet at ~0.36 μm (3.4 eV for GaN) or 0.2 μm (6.2 eV for AlN). The continuous range of bandgap energies now spans the near infrared, raising the possibility of new applications for group-III nitrides. In this article we present a detailed review of the physical properties of InN and related group III-nitride semiconductors. The electronic structure, carrier dynamics, optical transitions, defect physics, doping disparity, surface effects, and phonon structure will be discussed in the context of the InN bandgap re-evaluation. We will then describe the progress, perspectives, and challenges in the developments of new electronic and optoelectronic devices based on InGaN alloys. Advances in characterization and understanding of InN and InGaN nanostructures will also be reviewed in comparison to their thin film counterparts. *© 2009 American Institute of Physics*. [DOI: 10.1063/1.3155798]

TABLE OF CONTENTS

I. INTRODUCTION

The optoelectronics market is currently at 20 billion dollars per year, and is projected to rapidly expand further in the next few decades. This is driven largely by growth and advances in the sectors of solid state lighting and laser technologies. This growth was catalyzed by the introduction in 1990s of high-brightness blue light emitting diodes (LEDs) with InGaN as the active layer.[1,2] Research in this field has

a)Electronic mail: wuj@berkeley.edu.

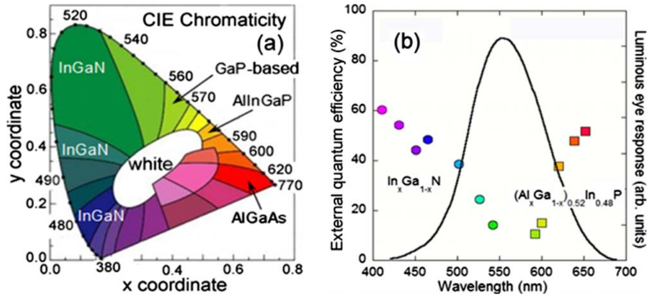

FIG. 1. (Color online) (a) The CIE chromaticity diagram, where the wavelength is given in nm and main LED materials are shown. (b) The external quantum efficiency of commercial $In_xGa_{1-x}N$ and $(Al_xGa_{1-x})_{0.52}In_{0.48}P$ LEDs (points) shown together with the luminous human eye response (curve). Reference 3.

thus been heavily focused on Ga-rich InGaN and GaAlN alloys, whose bandgaps cover the blue and near-ultraviolet parts of the electromagnetic spectrum. Since then, the rapid development of solid state lighting technology has revolutionized the fields of optoelectronics and optics. Figure 1(a) shows the widely adopted International Commission on Illumination chromaticity diagram that relates the color of light to human eye response. As seen in this diagram, InGaN plays a dominant role in the fields covering from the blue to the green, corresponding to 400–530 nm in wavelength, or 3.1 to 2.3 eV in photon energy. The In molar fraction in these materials is limited to $<\sim 0.3$. At higher In contents the external quantum efficiency (EQE) of LEDs rapidly drops to an unacceptable level,[3] an effect widely known as the "green valley of death" [Fig. 1(b)].[4,5]

On the other hand, much less effort has been devoted to InN and In-rich alloys. Earlier InN samples were synthesized using radio-frequency sputtering.[6] In most cases, this or similar methods produced polycrystalline samples with high free electron concentrations ($>10^{19}$ cm^{-3}) (Ref. 7) and significant oxygen contamination.[8] Such materials typically showed relatively low electron mobilities in the range of 10–100 $cm^2/V\ s$. The optical absorption measured in these samples showed a strong absorption band in the infrared and an absorption edge at about 1.9 eV.[9] The absorption band was attributed to impurity and free carrier absorption, and the value of 1.9 eV was thus widely quoted as the bandgap of intrinsic InN.[10] One of the unexplained characteristics, however, was the lack of light emission at or near the purported band edge. This was in stark contrast to GaN and Ga-rich InGaN, which show a strong luminescence despite very large concentrations of point and extended defects typical for these materials.[11]

Since then, the quality of nitride films has improved drastically with the availability of InGaN and InAlN films grown by metal-organic chemical vapor deposition (MOCVD). Correspondingly, a tremendous amount of effort has been put into the optical characterization of these films. The increased quality has translated to lower free carrier concentrations associated with unintentional doping, allowing the fundamental optical properties to be deconvoluted from band-filling dominated characteristics. Unexpectedly, it was discovered that the bandgaps of InGaN decrease very rapidly with increasing In content, and fall well below 2 eV for compositions approaching an In fraction of 0.5.[12,13] The rapid reduction of the bandgap versus the In molar fraction was attributed to a unusually large bandgap bowing parameter.[12]

The major breakthrough came about as a result of improved quality of InN films grown using molecular beam epitaxy (MBE).[14–16] Growth of thick InN films with much reduced free electron concentrations ($<10^{18}$ cm^{-3}) and high electron mobilities (>2000 $cm^2/V\ s$) was essential to the progress in understanding the properties of this material. The room-temperature fundamental bandgap of this type of high-quality InN was measured to be near 1.5 and 1.1 eV,[17] 0.9 eV,[15] 0.77 eV,[18] 0.7–1.0 eV,[19] 0.7 eV,[20] and finally converged to 0.64 eV.[21]

In this paper we review studies of In-rich group III-nitride alloys in the context of this discovery. It is shown that the newly discovered low value of the energy gap of InN provides a basis for a consistent description of the electronic structure of InN as well as the InGaN and InAlN alloys over the entire composition range. It is the aim of this review to present an up-to-date summary of physical parameters of group III-nitride semiconductors and their alloys. In Sec. II we discuss the narrow bandgap of InN and its related physical properties. This is followed by Sec. III with focus on properties of group III-nitride alloys and Sec. IV on their applications. Finally in Sec. V we summarize recent results obtained with group III-nitride nanostructures. This review is focused on wurtzite-structured nitrides, but zincblende nitrides will also be discussed. Topics not covered in this review are the growth, processing and structural properties of group-III nitrides. We refer interested readers to Refs. 22 and 23 for these topics.

II. NARROW BANDGAP OF InN

A. Optical properties

InN is more difficult to grow than GaN due to its low dissociation temperature ($\sim 630\ °C$) and high equilibrium vapor pressure of nitrogen. Nevertheless, in recent years considerable progress has been made in growth of high-quality wurtzite InN films by MBE (Refs. 14–16) and MOCVD.[23–27] Under ambient conditions group-III nitrides crystallize in the thermodynamically stable hexagonal wurtzite phase with the space group $P6_3mc$ (C_{6v}^4). MBE growth of InN in cubic zincblende structure with the space group $F\bar{4}3m$ (T_d^2) has also been reported.[28–31] At a hydrostatic pressure of ~ 12 GPa, InN undergoes a first-order structural phase transition from the wurtzite into the rocksalt structure with the space group $Fm3m$ (O_h^5).[32]

Figure 2 shows the optical characteristics of a high-quality wurtzite InN film grown by Lu *et al.*[33] using migration-enhanced MBE and measured by Wu *et al.*[21] The free electron concentration is 3.5×10^{17} cm^{-3} and the electron mobility is 2050 $cm^2/V\ s$ for the film. The optical absorption curve shows a strong onset slightly below 0.7 eV. The optical absorption coefficient rapidly increases to $\sim 10^4$ cm^{-1} above the onset, typical absorption intensity for direct bandgap semiconductors. There is no bandgap feature in the 1.8–2.0 eV region, i.e., in the energy range of previ-

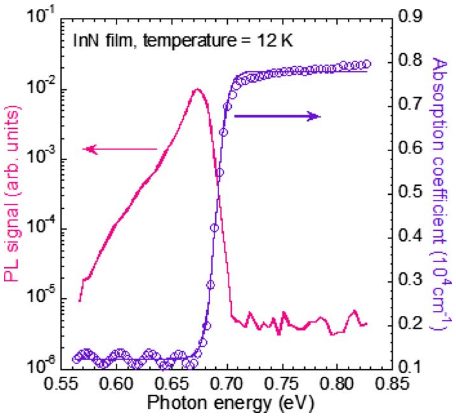

FIG. 2. (Color online) Absorption and photoluminescence of a high-quality, intrinsic InN film measured at 12 K. The solid line through the absorption data points is a sigmoidal fit. Reference 21.

ously reported values for the bandgap. The sample exhibits intense photoluminescence (PL) near the optical absorption edge, with a long tail toward the low energy side. The PL signal weakens with increasing temperature, but is detectable even at room temperature. At low temperatures, a photomodulated reflectance (PR) spectrum was also observed[18] which shows a transition feature at the same energy with a profile that is characteristic for interband transitions in a direct bandgap semiconductor. The simultaneous observations of the absorption edge, the PL, and the PR features at essentially the same energy indicate that this energy position corresponds to the optical transition across the fundamental bandgap of InN.

Both the PL peak and absorption edge exhibit a redshift with increasing temperature (Fig. 3), consistent with the expected behavior of a direct bandgap semiconductor.[21] The absorption edge shifts to lower energies by ~47 meV as temperature is increased from 12 K to room temperature. This change is significantly smaller than that of other group-III nitrides.[34] Also noted in Fig. 3, the absorption edge differs from the PL peak with decreasing temperature (~16 meV at low temperature). This difference can be attributed to the fact that the low-temperature PL is associated with transitions from low-density band-tail states, whereas the absorption edge is determined by the large-density band states. This difference is also sample specific, indicating that the shift of the PL peak energy cannot be used to accurately determine the behavior of the fundamental bandgap of InN.

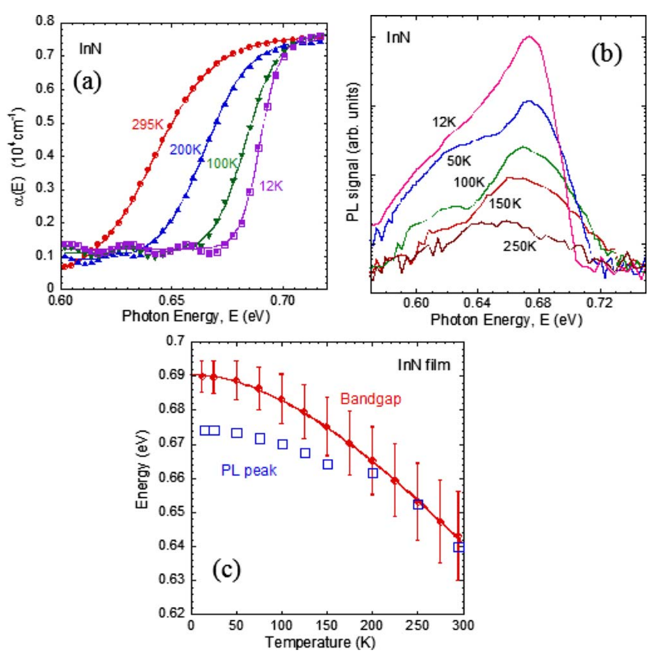

FIG. 3. (Color online) Absorption (a) and PL (b, log scale) spectra of InN measured at a wide range of temperatures. Panel (c) shows the temperature dependence of the PL peak and the bandgap determined from the absorption curves. The solid curve shows a fit to the bandgap with the standard Varshni's equation. Reference 21.

The temperature dependence of the direct bandgap is well described by Varshni's equation,

$$E_g(T) = E_g(0) - \frac{\alpha T^2}{\beta + T}. \tag{1}$$

The optical parameters of InN determined in this work are compared to those of GaN and AlN in Table I. It can be seen that all these parameters show a monotonic chemical trend from AlN to GaN and to InN. In the Varshni's equation, β is physically associated with the Debye temperature of the crystal. The value of $\beta = 454$ K for InN is consistent with the calculated range of Debye temperature for InN between 370 and 660 K.[48] α is much smaller than that of GaN and AlN, which suggests that the overall influence of thermal expansion and electron-phonon interaction on the fundamental bandgap is much weaker in InN. This is expected considering the larger ionicity and weaker bonding in InN compared to AlN and GaN.

These optical characteristics were obtained from c-plane wurtzite InN films grown on (0001) sapphire substrates. A power law dependence of the integrated PL intensity on the excitation power (Fig. 4) was reported. The power law is obeyed with a constant, near-unity index over a large range of excitation power, free electron concentrations, and temperatures.[49] This behavior is consistent with an exciton-mediated electron-hole recombination mechanism. In comparison, Fig. 5(a) shows the PL spectra of an a-plane $(11\bar{2}0)$ InN film grown on an r-plane sapphire.[50] A strong emission is observed at similar photon energies as in the c-plane InN. The PL signal is polarized when emitted from an a-plane film, as expected from a wurtzite crystal. Figure 5 shows the polarization dependence of the PL and absorption recorded with a polarizer rotating with respect to the c-axis.[50] The PL polarization anisotropy is an intrinsic property of crystalline materials. In the case of wurtzite InN, the PL anisotropy mimics the anisotropy of the hexagonal crystal structure, because the latter defines the symmetry and angular momentum of the electron wave functions, leading to polarization-dependent selection rules in interband optical transitions. The energy difference in the absorption edge for $E \perp c$ and $E \| c$ polarizations [Fig. 5(b)] is related to the crystal-field and spin-orbit splits at the Γ point in the valence bands.[44] A quantitative interpretation of these anisotropic effects requires the inclusion of possible biaxial strain in the film induced by the lattice mismatch with the substrate.[51] This well-

TABLE I. Recommended values of basic physical parameters of wurtzite InN, AlN, and GaN. Values not referenced were calculated from commonly accepted parameters.

Parameter	AlN	GaN	InN
Lattice constant a ($T=300$ K) (nm)	0.3112[a]	0.3189[a]	0.3533[a]
Thermal expansion $d \ln a/dT$ (10^{-6}/K)	4.2[a]	5.6[a]	3.8[a]
Lattice constant c ($T=300$ K) (nm)	0.4982[a]	0.5185[a]	0.5693[a]
Thermal expansion $d \ln c/dT$ (10^{-6}/K)	5.3[a]	3.2[a]	2.9[a]
Density (g/cm^3)	3.23[a]	6.15[a]	6.81[a]
Phillips ionicity	0.449[b]	0.500[b]	0.578[b]
Debye temperature (K)	1150[a]	600[a]	660[a]
Melting point (K)	3487[c]	2791[c]	2146[c]
Decomposition temperature (°C)	1040[c]	850[c]	630[c]
Decomposition activation energy (kJ/mol)	414[c]	379[c]	336[c]
Static dielectric constant, $\varepsilon_S/\varepsilon_0$	8.5[a]	8.9[a]	10.5[d]
High-frequency dielectric constant, $\varepsilon_\infty/\varepsilon_0$	4.6[a]	5.4[a]	6.7[e]
Bandgap $E_g(T=0)$ (eV)	6.25[f]	3.51[f]	0.69[g]
Bandgap $E_g(T=300$ K) (eV)	6.14[f]	3.43[f]	0.64[g]
Vashni parameter α (meV/K)	1.799[f]	0.909[f]	0.414[g]
Vashni parameter β (K)	1462[f]	830[f]	454[g]
Electron Effective mass at band edge m_e^*/m_0	0.32[f]	0.20[f]	0.07[h]
Exciton binding energy (meV)	60	34	9
Exciton Bohr radius (nm)	1.4	2.4	8
Mg acceptor binding energy (eV)	0.51[i]	0.17[i]	0.06[j]
Critical point A (eV), $U_3 \to U_3$		6.36[k]	4.88[k]
Critical point E_1 (eV), $L_{2,4} \to L_{1,3}$, $M_4 \to M_{1,3}$	7.97[k]	7.00[k]	5.35[k]
Critical point E_2 (eV), $H_3 \to H_3$, $M_2 \to M_1$	8.95[k]	7.96[k]	6.05[k]
Critical point E_3 (eV), $K_{2,3} \to K_2$		9.25[k]	7.87[k]
A_1(TO) phonon (1/cm)	611[l]	532[l]	447[l]
A_1(LO) phonon (1/cm)	890[l]	734[l]	586[l]
E_1(LO) phonon (1/cm)	912[l]	741[l]	593[l]
E_1(TO) phonon (1/cm)	671[l]	559[l]	476[l]
E_2^H phonon (1/cm)	657[l]	568[l]	488[l]
E_2^L phonon (1/cm)	249[l]	144[l]	87[l]

[a]Reference 35.
[b]Reference 36.
[c]Reference 37.
[d]Reference 38.
[e]Reference 39.
[f]Reference 40.
[g]Reference 21.
[h]Reference 20.
[i]Reference 41.
[j]Reference 42.
[k]References 43–46.
[l]Reference 47.

behaved optical anisotropy is an indication of the interband nature of the optical transitions near 0.64 eV. The PL peak energy of both the a-plane[52] and the c-plane[49] films exhibits a blueshift with increasing excitation power, which can be attributed to the increasing population of the conduction and valence bands by photocarriers at more intense excitation power.

B. Band structure

1. k·p calculations of conduction band

A direct consequence of the narrow gap of InN is the strong nonparabolicity of the lowest conduction band. It is well known that for narrow direct-gap semiconductors such as InSb and InAs,[53] the dispersion at the bottom of the conduction band takes a nonparabolic form as a result of the $\boldsymbol{k}\cdot\boldsymbol{p}$ repulsion across the narrow gap between the conduction and valence bands. The problem can be treated analytically using an 8×8 $\boldsymbol{k}\cdot\boldsymbol{p}$ Hamilton matrix that describes the electron wave functions of the p-like valence bands and the s-like conduction band.[54]

The spin-orbit splitting Δ_{so} in a compound semiconductor is comparable to the atomic spin-orbit splitting of its anion valence electrons, which is typically small for light atoms.[54] group-III nitrides thus have extremely small Δ_{so} ($<$room-temperature k_BT), as listed in Table II. Neglecting Δ_{so} and the spin degree of freedom, the 8×8 $\boldsymbol{k}\cdot\boldsymbol{p}$ Hamilton matrix reduces to a 4×4 one. Choosing the electronic wave functions $|iS\rangle$, $|-X+iY/\sqrt{2}\rangle$, $|X-iY/\sqrt{2}\rangle$, and $|Z\rangle$ as the basis, the matrix is written as[55]

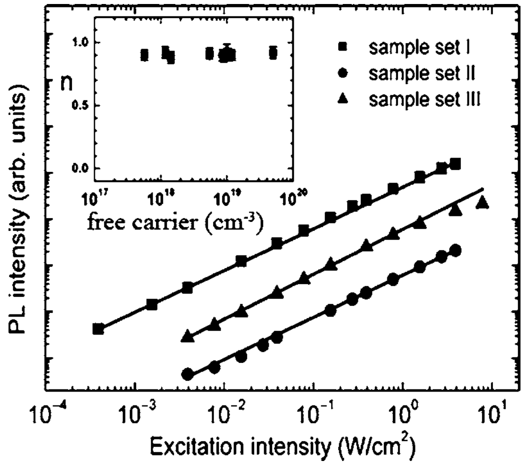

FIG. 4. Integrated PL intensity as a function of excitation intensity for a c-plane InN film. The solid lines are power law fits. The inset shows the power law index being a constant independent of free electron concentration. Reference 49.

$$H = \frac{\hbar^2 k^2}{2m_0} + \begin{pmatrix} E_g + \Delta_{cr} & iP_{xy}k_x & iP_{xy}k_y & iP_z k_z \\ -iP_{xy}k_x & \Delta_{cr} & 0 & 0 \\ -iP_{xy}k_y & 0 & \Delta_{cr} & 0 \\ -iP_z k_z & 0 & 0 & 0 \end{pmatrix} + H_{remote}, \tag{2}$$

where H_{remote} describes the influence from remote bands, and P_{xy} and P_z are the momentum matrix elements defining the $\boldsymbol{k}\cdot\boldsymbol{p}$ interaction,

$$P_{xy} = \frac{\hbar}{2m_0}\langle S|\frac{\hbar}{i}\frac{\partial}{\partial x}|X\rangle = \frac{\hbar}{2m_0}\langle S|\frac{\hbar}{i}\frac{\partial}{\partial y}|Y\rangle; \tag{3a}$$

$$P_z = \frac{\hbar}{2m_0}\langle S|\frac{\hbar}{i}\frac{\partial}{\partial z}|Z\rangle. \tag{3b}$$

We further neglect the crystal-field splitting Δ_{cr} (<40 meV for InN) and H_{remote} (remote bands are at least 4 eV away), and assume an isotropic band structure at small k so that $P_{xy} \approx P_z$. With these simplifications the Hamiltonian in Eq. (2) can be diagonalized with the following eigenvalue obtained for the conduction band dispersion,[20]

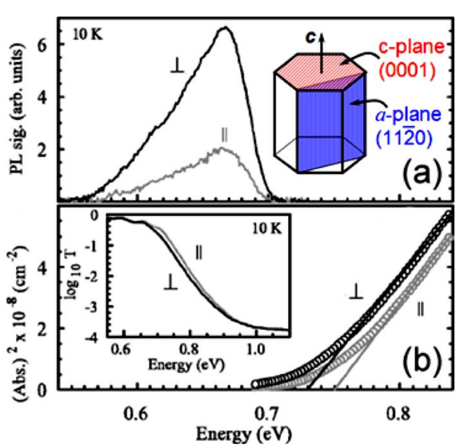

FIG. 5. (Color online) (a) PL spectra of an a-plane InN film with $E \perp c$ and $E \parallel c$ polarization, respectively. (b) Measured absorption coefficient squared of the a-plane film as a function of photon energy for the two polarizations. The inset shows the full transmission spectra. Reference 50.

$$E_C(k) = E_g + \frac{\hbar^2 k^2}{2m_0} + \frac{1}{2}\left(\sqrt{E_g^2 + 4E_P \cdot \frac{\hbar^2 k^2}{2m_0}} - E_g\right). \tag{4}$$

Here $E_g = 0.64$ eV is the intrinsic bandgap, m_0 is the electron mass in vacuum, and $E_P = (2m_0/\hbar^2)|P_z|^2$ is the $\boldsymbol{k}\cdot\boldsymbol{p}$ interaction energy. $E_C(k)$ is referenced to the valence band maximum.

As shown in Eq. (4), the nonparabolicity of the conduction band is more pronounced for small E_g (i.e., narrow-gap semiconductors) or large E_P, because the conduction band feels stronger perturbation from the valence bands when E_g is smaller or E_P is larger. At very small k values (i.e., near the Γ point), Eq. (4) is simplified into a parabolic band,

$$E_C(k) \approx E_g + \frac{\hbar^2 k^2}{2m_e^*(0)}, \tag{5}$$

where the effective electron mass at the Γ-point conduction band minimum is

$$\frac{m_e^*(0)}{m_0} = \left(1 + \frac{E_P}{E_g}\right)^{-1}. \tag{6}$$

Figure 6 shows the calculated conduction and valence band dispersion using Eq. (4) (nonparabolic) and Eq. (5) (parabolic), respectively. The parabolic dispersion deviates severely from the nonparabolic one when $k > \sim 0.05/\text{Å}$, or, as shown below, when the electron concentration $n > \sim 10^{19}$ cm^{-3} so that the Fermi level (E_F) is displaced deep into the conduction band.

In the case of degenerate doping, optical absorption is forbidden for transitions below the Fermi surface. Therefore, the onset of the optical absorption would overestimate the intrinsic bandgap, leading to an effect known as the Burstein–Moss effect.[65] Optical emission below the Fermi surface, such as PL, would be still possible but significantly broadened compared to the intrinsic band edge emission, as illustrated schematically in Fig. 6.[20] This implies that for heavily doped semiconductors, such as earlier, sputter-grown InN films, the absorption and luminescence spectra should be interpreted with caution.[66]

The Burstein–Moss shift illustrated in Fig. 6 well explains the discrepancy between the earlier 1.9 eV and the newly established 0.64 eV bandgap. High-quality InN films have been grown by MBE where the free electron concentration is varied over several orders of magnitude by controlled Si doping.[65] The absorption edge was determined from optical absorption experiments as a function of free electron concentration. The absorption edge, or sometimes referred to as the "optical bandgap," varies continuously from 0.64 eV, the intrinsic bandgap of InN, to ~2 eV for samples with $n > 5 \times 10^{20}$ cm^{-3}.[65] Bandgaps of earlier, sputter-grown InN films fall accurately onto this dependence, and are therefore well explained by the Burstein–Moss effect. The high free electron concentrations originate from unintentional dopants such as oxygen and native defects.

TABLE II. Physical parameters of wurtzite InN, AlN, and GaN. Values are theoretical except those in parenthesis which are experimental values.

Parameter	AlN	GaN	InN
Δ_{cr} (meV)	-169[a]	10[a]	40[a]
Δ_{so} (meV)	19[a]	17[a]	5[a]
$m_e^{\parallel}/m_0$	0.32[b]	0.19[b]	0.065[b]
$m_e^{\perp}/m_0$	0.33[b] (0.29–0.45)	0.21[b] (0.20–0.22)	0.068[b] (0.03–0.085)[c]
$m_A^{\parallel}/m_0$	0.26[a]	1.89[a] (1.76)	1.56[a]
$m_A^{\perp}/m_0$	3.99[a]	0.26[a] (0.35)	0.17[a]
$m_B^{\parallel}/m_0$	3.57[a]	0.44[a] (0.42)	1.54[a]
$m_B^{\perp}/m_0$	0.64[a]	0.33[a] (0.51)	0.17[a]
$m_C^{\parallel}/m_0$	3.54[a]	0.18[a] (0.30)	0.12[a]
$m_C^{\perp}/m_0$	0.64[a]	0.74[a] (0.68)	1.46[a]
A_1	-3.86[a]	-7.21[a]	-8.21[a]
A_2	-0.25[a]	-0.44[a]	-0.68[a]
A_3	3.58[a]	6.68[a]	7.57[a]
A_4	-1.32[a]	-3.46[a]	-5.23[a]
A_5	-1.47[a]	-3.40[a]	-5.11[a]
A_6	-1.64[a]	-4.90[a]	-5.96[a]
A_7 (eV·Å)	0[a]	0.0937[a]	0[a]
Volume deformation potential, a_V (eV)	-10.2[d]	-7.4[d]	-3.7[d]
Bulk modulus, B (kbar)	2158[d] (1850–2079) [b]	2063[d] (1880–2450)[b]	1498[d] (1260–1480)[b]
dE_g/dP (meV/kbar)	4.0[e]–4.2[f] (4.9[g])	3.1[f]–3.9[e] (3.9[h])	1.8[f]–3.3[e] (2.7–3.0)[i]
$E_P^{\parallel}$ (eV)	17.0[j]	17.3[j] (17.8–18.7)[k]	8.7[j]
$E_P^{\perp}$ (eV)	18.2[j]	16.3[j] (16.9–17.8)[k]	8.8[j] 9.7–10[l]
d_{13} (pm/V)	-2.1[a]	-1.6[a]	-3.5[a]
d_{33} (pm/V)	5.4[a]	3.1[a]	7.6[a]
d_{15} (pm/V)	3.6[a]	3.1[a]	5.5[a]
P_{sp} (C/m^2)	-0.090[a]	-0.034[a]	-0.042[a]

[a]Reference 40.
[b]Reference 55.
[c]References 20, 38, 56, and 57.
[d]Reference 58.
[e]Reference 59.
[f]Reference 58.
[g]Reference 60.
[h]Reference 61.
[i]References 61–63.
[j]Reference 55.
[k]Reference 64
[l]Reference 56
[m]Reference 20.

Electron concentrations as high as 2×10^{21} cm^{-3} have been reported in InN. The extreme n-type propensity of InN is a direct consequence of its large electron affinity,[67] as will be discussed in Sec. III B.

The increase in absorption edge with increasing electron concentration was calculated by the dispersion relation in Eq. (4) (nonparabolic) or Eq. (5) (parabolic) evaluated at the Fermi wavevector $k_F=(3\pi^2 n)^{1/3}$, neglecting the thermal broadening of the Fermi distribution. In the calculation, the conduction band renormalization effects due to electron-electron interaction and electron-ionized impurity interaction are also taken into account.[20] The calculated dependences are compared to the experimental data and to each other in Fig. 7. The calculated optical bandgap assuming a parabolic conduction band shows a Burstein–Moss shift too fast to describe the experimental data.

The conduction band nonparabolicity results in a $\boldsymbol{k}$-dependent electron effective mass given by

$$m_e^*(k) \equiv \frac{\hbar^2 k}{dE_C(k)/dk}. \tag{7}$$

As k approaches 0, Eq. (7) gives the band minimum effective mass defined in Eq. (6). The electron effective mass of InN has been measured by several groups using various methods such as plasma reflection spectroscopy and infrared spectroscopic ellipsometry.[20,38,39,56,68,69] Values of $m_e^*(0)/m_0$ at 0.039–0.047,[70] 0.033,[57] 0.14,[39] 0.085,[38] 0.05,[56] 0.07,[20] and 0.24[69] have been reported. In the case of plasma reflection spectroscopy, infrared reflection curves are measured and fitted with a standard dielectric function model,

$$R(\omega) = \left| \frac{\sqrt{\varepsilon(\omega)}-1}{\sqrt{\varepsilon(\omega)}+1} \right|^2, \tag{8}$$

where the complex dielectric function is given by the classical dielectric function,

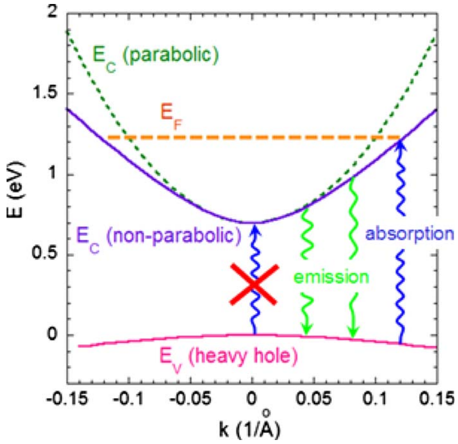

FIG. 6. (Color online) Calculated conduction and valence band dispersion of InN using the $\boldsymbol{k}\cdot\boldsymbol{p}$ model. The Fermi level for $n=10^{20}$ cm^{-3} is shown. Reference 20.

$$\varepsilon(\omega)/\varepsilon_\infty = 1 - \frac{\omega_p^2}{\omega^2 + i\omega\gamma}. \tag{9}$$

The reflection curves drop rapidly at the plasma frequency ω_p given by

$$\omega_p = \sqrt{\frac{ne^2}{\varepsilon_0\varepsilon_\infty m_e^*}}. \tag{10}$$

Here γ is the damping parameter related to carrier scattering which broadens the plasma reflection edge. The plasma edge shifts to higher energy as n is increased. The effective mass thus obtained is shown in Fig. 8 together with the values reported by different groups, and compared with calculated results of Eq. (7). It can be seen that although the data were measured by different groups for InN films grown by different methods, the calculations based on the nonparabolic conduction band using E_g=0.64 eV and $E_P\approx 10$ eV show a good agreement with all the measured values. Note that the same value of E_P=10 eV was also used in calculating the Burstein–Moss shift in Fig. 7. Therefore, a good consistent picture is established in describing the conduction band of InN based on the $\boldsymbol{k}\cdot\boldsymbol{p}$ model. The extrapolation of the curve

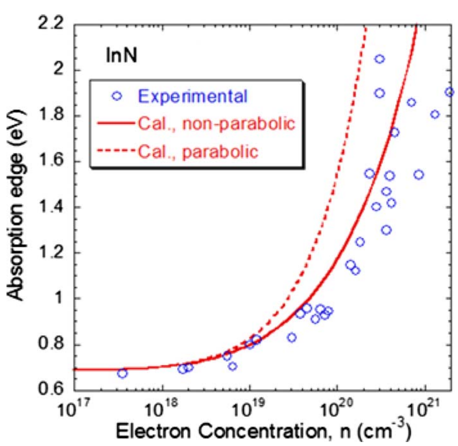

FIG. 7. (Color online) Absorption edge (optical bandgap) plotted as a function of electron concentration. The $\boldsymbol{k}\cdot\boldsymbol{p}$ calculated results are also shown. Reference 65.

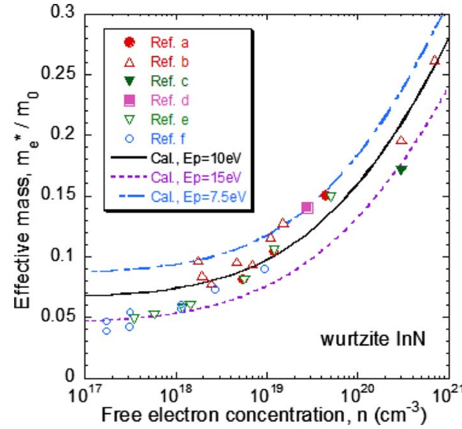

FIG. 8. (Color online) Effective electron mass as a function of electron concentration. The curves are calculated dependences based on the nonparabolic dispersion using different E_P values. References a 20, b 38, 68, and 69, c 7, d 39, e 56, and f 70.

in Fig. 8 leads to a small effective mass of $m_e^*(0)/m_0 = 0.07\pm 0.02$ at the bottom of the conduction band. This value agrees very well with recently calculated value between 0.065 and 0.068,[55] as will be discussed below. For other values, such as a smaller $m_e^*(0)/m_0\approx 0.05$ reported by Fu *et al.*, a larger $E_P\approx 15$ eV would be needed to fit with it. Recently Gorczyca *et al.*[71] studied the increase in $m_e^*(0)$ under hydrostatic pressure.

It has been argued that the interaction energy E_P is material insensitive and is nearly a constant, between 10 and 15 eV, close to the value expected in the empty lattice model.[54] This energy is much larger than E_g of most semiconductors. Therefore, according to Eq. (6), $m_e^*(0)$ is approximately proportional to the direct-gap E_g for group III-V and II-V semiconductors. In Fig. 9 we show this relationship where a universal E_P=12 eV was used. This dependence is approximately linear for small-E_g materials. Interestingly, previously reported $m_e^*=0.11m_0$ measured from sputter-grown InN films with "optical bandgap" at 1.9 eV also falls near this dependence.[7] This is because for those degenerately doped films, both m_e^* and E_g (the "optical bandgap") were

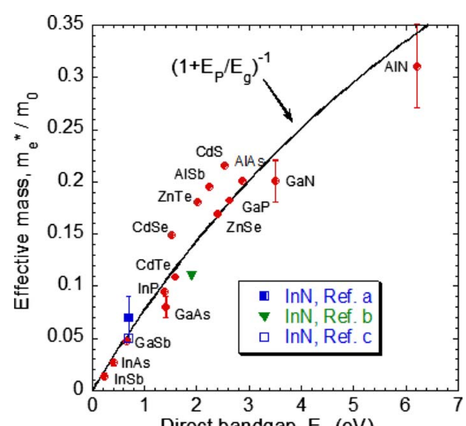

FIG. 9. (Color online) Effective electron mass at the conduction band minimum at the Γ point as a function of the Γ-point direct bandgap in various semiconductors. The solid line is a fit to Eq. (6) which leads to a universal E_P=12 eV. Refs: a 20, b 56, c 7.

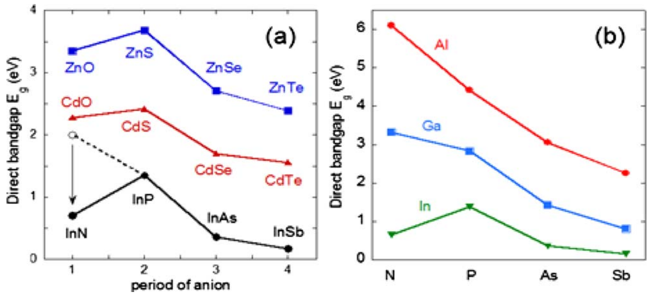

FIG. 10. (Color online) (a) The breakdown of the common-cation rule in Zn-VI, Cd-VI, and In-V semiconductors. (b) Trend of direct bandgaps in group III-V semiconductors.

measured at a Fermi level deep into the conductance band. In this case E_g is raised by the Burstein–Moss effect, but m_e^* is increased by the band nonparabolicity as well, and as a result they fall back at a position near the universal curve shown in Fig. 9.

2. First-principle calculations

This is not the first time in history that a much wider bandgap has been assigned erroneously to a semiconductor. For example, the fundamental bandgap of PbS had been believed to be 1.2 eV until in 1953 it was found to be only 0.4 eV.[72] The narrow bandgap of InN is more puzzling as it breaks the common-cation rule. The common-cation (anion) rule states that for isovalent, common-cation (anion) semiconductors, the direct gap at the Γ point increases as the anion (cation) atomic number decreases. The bandgap of InN at 0.64 eV is not only much smaller than the previously reported bandgap of InN but also smaller than the well-established bandgap of InP at 1.4 eV. However, the breakdown of the common-cation (anion) rule is not unusual in ionic semiconductors. As shown in Fig. 10(a), for Zn-group VI compounds the bandgap of ZnO is also smaller than that of ZnS.

According to the tight-binding model, the valence (conduction) band edge derives mainly from the bonding (antibonding) state of anion and cation p (s) atomic orbitals.[54] The energies of these orbitals for group III and V elements are shown in Fig. 11(a).[73] The N $2s$ orbital energy is at -18.5 eV, compared with P at -14.09 eV, and is much lower than the s orbital energy of any other element in the figure. This is the main reason that leads to an exceptionally low conduction band minimum (CBM) in InN, and the breakdown of the common-cation rule. The trend of the breakdown can be seen in Fig. 10(b).[74]

For the CBM of group III-N compounds, as the s energy does not differ much among Al, Ga, and In, the CBM is predominantly determined by the energy of the N $2s$ state and its weight in the CBM. Moving from AlN to GaN and to InN, the ionicity increases (Table I) and consequently the contribution of N $2s$ state increases, resulting in the lowest CBM in InN among all group III-V semiconductors. Similarly there are only very small differences in the p energy of Al, Ga, and In, and as such, the predominant factor in determining the valence band maximum (VBM) in III-N's is the interaction between the cation d orbitals and the N $2p$ orbital. This p-d repulsion pushes the VBM up in InN more than in GaN and AlN because the In $4d$ level is the highest. For common-cation, In-group V compounds, it can be seen that the trend of CBM and VBM largely follows the anion s and p energy, respectively. Due to the small electronegativity of In, the In s and p orbitals contribute much less to the CBM and VBM.

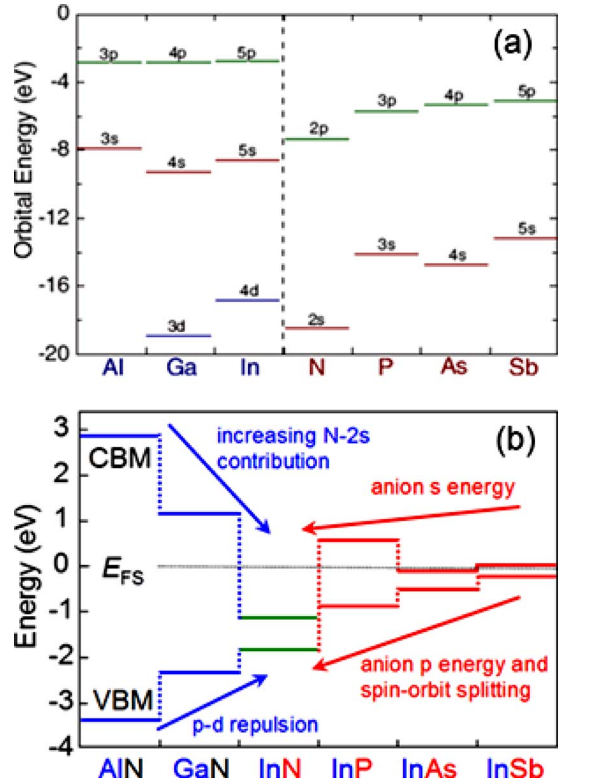

FIG. 11. (Color online) (a) Atomic orbital energies of group III and V elements. (b) conduction and valence band edges of related group III-V semiconductors with respect to E_{FS} (see Sec. III B). Reference 73.

The common-cation and common-anion rules cannot be accounted for by the pure chemical trend alone.[74] The atomic size or volume effect also plays an important role in determining the bandgap. Semiconductors crystallize at their respective equilibrium lattice constants, which are typically quite different from each other. Therefore, the size or volume deformation contribution to the bandgap has to be considered. The volume deformation potential a_V, i.e., the change in the bandgap with respect to a relative change in the volume, is typically negative; the direct bandgap thus increases when the lattice constant is reduced. Generally the order of the bandgaps calculated at fixed lattice constant is opposite to what is observed at the equilibrium lattice constants. The volume deformation contribution reverses this order and gives rise to the common-cation and common-anion rules. InN has a relative weak a_v (-4.2 eV) compared to other In–V compounds (e.g., -5.9 eV for InP) and III-N compounds (Table II). Therefore, the atomic size effect in InN is not strong enough to open the bandgap of InN, resulting in a smaller bandgap than InP and breakdown of the common-cation rule.[74]

First-principle calculations of the band structure have become a powerful tool to explain and predict material properties and design new materials. They also provide results to parametrize simplified methods, such as the analytical $\boldsymbol{k}\cdot\boldsymbol{p}$ method discussed previously. The latter are conveniently applicable to device modeling in the envelope function scheme at low computational expense. First-principle calculations of InN have been made long before the discovery of its narrow bandgap using the standard density functional theory in the local density approximation (LDA).[75–77] However, it is well known that although LDA well predicts structural parameters such as the equilibrium lattice constant, it typically severely underestimates the bandgap of semiconductors, due mostly to an incomplete cancellation of artificial self-interaction. For example, the LDA-calculated bandgap of GaAs is only ~0.3 eV,[77] much smaller than the experimental value of 1.52 eV at zero temperature. For InN in the wurtzite structure, LDA predicts a metallic state with a bandgap of ~ −0.3 eV.[75–77] Various methods have been attempted to correct the LDA bandgap error. Using the screened exchange approach, Schilfgaarde *et al.* find that the bandgaps are 1.3 and 1.4 eV for zincblende and wurtzite InN, respectively.[76] Model GW calculation by Johnson and Ashcroft yields a bandgap of 1.79 eV for InN.[78] Using the self-interaction correction, Vogel *et al.* find a corrected bandgap of 1.6 eV for the wurtzite InN.[79] Quasiparticle calculation using the *GW* approximation gives a bandgap value of only 0.01 eV (Ref. 77) or 0.02–0.05 eV.[80]

More efforts have been devoted to the band structure calculation of InN after the experimental discovery of its narrow bandgap. Using a LDA-based semiempirical method,[74,81] Wei *et al.* calculated the bandgap of InN and systematically studied the chemical trends of the bandgap and other band parameters in group-III nitrides. Bandgaps of 0.70 and 0.85 eV was found for zincblende and wurtzite InN, respectively. In their approach they correct the LDA bandgap error by adding to the LDA potential a δ-function-like external potential inside the muffin-tin spheres, and perform the calculation self-consistently. The bandgap obtained by this method is much closer to the real value. Alternatively, using a special type of pseudopotentials which account for self-interaction corrections, Bechstedt and Furthmueller obtained a bandgap of 0.59 and 0.81 eV for zincblende and wurtzite InN, respectively;[82] Bagayoko *et al.* obtained a bandgap of 0.65 eV (Ref. 83) and 0.88 eV (Ref. 84) for zincblende and wurtzite InN, respectively.

Very recently, Rinke *et al.*[55] employed a single-iteration *GW* method based on density functional theory to determine the basic band parameters of group-III nitrides. Their calculations were carried out at the experimental lattice constants; their method is fully self-interaction free and therefore expected to effectively correct the LDA error. A consistent set of band parameters were found for AlN, GaN, and InN. Specifically, the fundamental bandgap of InN was calculated to be 0.69 and 0.53 eV for the wurtzite and zincblende phases, respectively. As these values are the closest to experimental data, we recommend their calculated band parameters in Tables I and II. Their calculated conduction and valence bands in the vicinity of the Γ point are shown in Fig. 12. These bands are very well reproduced by the $\boldsymbol{k}\cdot\boldsymbol{p}$ formulation if the recommended band parameters in Table II are

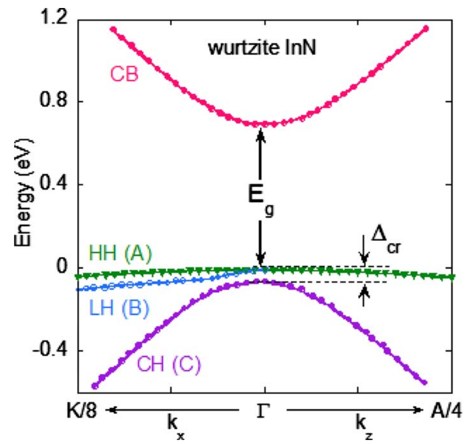

FIG. 12. (Color online) First-principle calculation of the conduction and valence bands of wurtzite InN near the Γ point. Analytical dispersions using $\boldsymbol{k}\cdot\boldsymbol{p}$ parameters listed in Table II agree well with these curves. Reference 55.

used.[55] Compared to the $\boldsymbol{k}\cdot\boldsymbol{p}$ calculated bands shown in Fig. 6, it can be seen that the calculated E_g=0.69 eV, m_e^*/m_0 =0.065 (∥) or 0.068 (⊥), and E_P=8.7 eV (∥) or 8.8 eV (⊥), all agreeing very well with up-to-date experimental values E_g=0.69 eV, m_e^*/m_0=0.07, and E_P=10 eV. In addition, the first-principle calculations provide many band parameters that are not yet experimentally available, such as the crystal-field splitting and spin-orbit splitting, deformation potentials, and the hole effective masses. These parameters are listed in Table II.

Most of these theoretical works only present the band structure near the Γ point or along the Γ-*M* and Γ-*A* lines. Figure 13 shows the band structure of InN in the entire Brillouin zone calculated by Fritsch *et al.* within the empirical pseudopotential method by exploiting the transferability of ionic model potential parameters.[85] Their calculation gives bandgap values of 0.79 and 0.59 eV for wurtzite and zincblende InN, respectively. From these dispersion curves, critical points at higher energies can be also identified. These critical points correspond to direct optical transitions with high transition probabilities. These transitions typically occur at Van Hove singularities in the joint conduction-valence band density of states where $E_C(k)-E_V(k)$ takes a local minimum,[54]

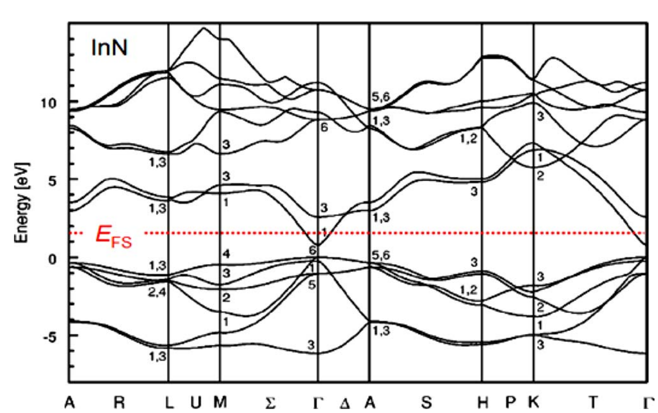

FIG. 13. (Color online) First-principle calculation of the band structure of wurtzite InN in the entire Brillouin zone. The Fermi stabilization level (E_{FS}) is also shown (see Sec. III B). Reference 85.

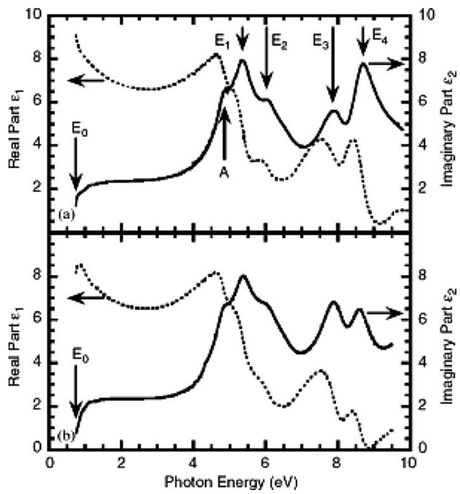

FIG. 14. Experimentally measured real (dashed line) and imaginary (full line) part of the ordinary dielectric function of wurtzite InN as determined from c-plane (a) and a-plane (b) films. Critical points are marked by arrows. Reference 44.

$$D_{\mathrm{joint}}(E_C - E_V) \sim \int \frac{dS_{\mathbf{k}}}{|\nabla_{\mathbf{k}}[E_C(\mathbf{k}) - E_V(\mathbf{k})]|}. \quad (11)$$

Experimentally these critical point energies can be determined from the complex dielectric functions measured in the 0–10 eV range using ellipsometry.[44,45,86] Such a set of experimental dielectric function curves are shown in Fig. 14.[44] In addition to the direct bandgap (E_g or E_0) at ~0.7 eV, five critical points are clearly seen at energies 4.88, 5.35, 6.05, 7.87, and 8.70 eV, respectively. They are determined by fitting the dielectric function curves with a third-derivative line shape,[44] and labeled as transition A, E_1, E_2, E_3, and E_4, respectively (after Ref. 87). These energies agree well with calculations in Fig. 13 if the assignments listed in Table I are used.[88] Unlike the blueshift of the bandgap due to the Burstein–Moss effect, these energies were found to be independent of the doping level.[88] This is expected from the fact that these energies involve optical transitions deep in the conduction and valence bands far from the Fermi level. In Sec. III A we will discuss the composition dependence of these critical points in InGaN and InAlN alloys.

The zincblende structure differs from the wurtzite one only in its third-nearest-neighbor atomic arrangement; consequently these two structures are quite close in total energy.[75] The direct bandgap of a wurtzite semiconductor is typically ~0.1 eV wider than its zincblende polymorph. Schoermann *et al.* grew zincblende InN using MBE and measured the bandgap to be 0.61 at low temperature and 0.56 at room temperature.[89] These values are recommended and listed together with other physical properties of zincblende group-III nitrides in Table IV.

C. Carrier recombination dynamics

The understanding of the physics and dynamics of carrier recombination is crucial for the development of InN-based devices. The recombination physics can be studied by various time-resolved pump-probe techniques. Figure 15(a) shows the differential transmission transients of three InN

TABLE III. Recommended values of basic physical parameters of interfaces and alloys between wurtzite InN, AlN and GaN.

Parameter	AlN–GaN	GaN–InN	InN–AlN
Valence band offset, ΔE_v (eV)	-0.7^{a}	-1.1^{a}	1.8^{a}
Alloy bandgap bowing (eV)	0.6^{b}	1.4^{c}	5.0^{d}
Alloy critical point A bowing (eV)		0.8^{e}	
Alloy critical point E_1 bowing (eV)	0.2^{e}	1.1^{e}	1.8^{e}
Alloy critical point E_2 bowing (eV)	0.1^{e}	1.0^{e}	2.7^{e}
Alloy critical point E_3 bowing (eV)	0.5^{e}	0.7^{e}	

[a]Reference 105.
[b]Reference 106.
[c]Reference 95.
[d]Reference 94.
[e]References 43–46.

films with distinctly different doping levels reported by Chen *et al.*[90] The probe energy was tuned to the absorption edge (E_g). The pump pulse is shorter than 1 ps and its intensity was controlled such that the injected carrier density is much lower than the original equilibrium carrier concentration in the sample. It is clear that these transients can be described by a single exponential decay, with a nonequilibrium carrier lifetime (τ) depending on doping level and temperature. Similar dynamics was also probed using transient photoreflectance technique.[91] The room-temperature carrier lifetime determined in these studies is plotted together as a function of the electron concentration in Fig. 15(b). It can be seen, not surprisingly, that the carrier lifetime is approximately inversely proportional to the free electron concentration. This effect is analogous to the rapid decrease in electron mobility with increasing electron concentration in InN;[92] both effects are dependent on impurities and defects, which scatter free carriers (in the case of electrical transport) or mediate carrier recombination (in the case of optical transitions).

The photogenerated electrons and holes recombine mainly through three channels: nonradiative defect-mediated, radiative interband, and nonradiative Auger recombination. The total recombination rate is written as

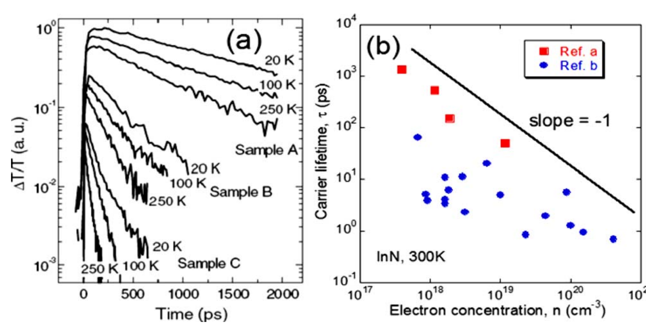

FIG. 15. (Color online) (a) Differential transmission of three InN samples with different electron concentrations under a pump fluence of 1 μJ/cm^2. Electron concentration: sample A: 1.3×10^{18} cm^{-3}, sample B: 2.7×10^{18} cm^{-3}, and sample C: 1.2×10^{19} cm^{-3}. Reference 90. (b) Recombination lifetime vs carrier concentration. The samples with high electron concentrations ($>2\times10^{19}$ cm^{-3}) were Si-doped, while the rest were not intentionally doped. References a 90 and b 91.

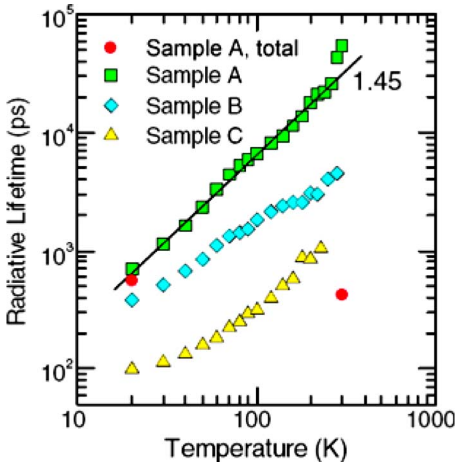

FIG. 16. (Color online) Radiative lifetime ($\tau_{\text{radiative}}$) of carriers in InN as a function of temperature. The solid line indicates a power law fit to sample A. The two red dots show the measured total lifetime (τ) in sample A. Reference 90.

$$\frac{1}{\tau} = \frac{1}{\tau_{\text{defect}}} + \frac{1}{\tau_{\text{radiative}}} + \frac{1}{\tau_{\text{Auger}}} = \sigma \bar{v} N_{\text{defect}} + B_{\text{radiative}} n + B_{\text{Auger}} n^2, \tag{12}$$

where σ and $\bar{v}$ are the capture cross section and mean velocity of free carriers, respectively. The fact that the overall slope of τ versus n is closer to -1 than to -2 in Fig. 15(b) suggests that the Auger effect is not a dominant recombination mechanism in InN, at least not for the pumping intensities used in these experiments.

Using Eq. (12), Chen *et al.* estimated the radiative recombination coefficient to be $B_{\text{radiative}} = (2.6 \pm 0.5) \times 10^{-11}$ cm^3 s^{-1} at 300 K for InN.[90] By relating the temperature dependence of PL intensity to the radiative recombination rate, they further extracted the temperature-dependent radiative recombination lifetime, $\tau_{\text{radiative}}$, as shown in Fig. 16, where the total lifetime (τ) at 20 and 300 K for sample A are also shown for comparison. It is clear from Fig. 16 that the defect-mediated nonradiative recombination is largely inactive at low temperatures, while it becomes dominant at higher temperatures. The derived $\tau_{\text{radiative}}$ is strongly temperature dependent and scales with $\sim T^{\gamma}$, where γ is close to 3/2. This is consistent with the Lasher–Stern model which predicts that for bimolecular radiative recombination in direct bandgap semiconductors, $B_{\text{radiative}} \sim T^{-3/2}$ when the momentum selection rule holds.[90]

Analyzing the differential transmission transient in Fig. 15(a) in energy (rather than time) domain reveals that although the signal at peak and lower energies exhibits a single-exponent decay which is recombination related, for the high-energy shoulder, a fast decay ($\sim$10 ps) occurs prior to this carrier recombination [Fig. 17(a)].[93] This fast decay is attributed to hot-carrier thermalization. Assuming a Maxwell–Boltzmann distribution of hot electrons and holes, the carrier temperature can be derived from the slope of the high-energy shoulder in Fig. 17(a). The carrier temperature obtained by this means is plotted as a function of time in Fig. 17(b), showing a cooling of photoexcited carriers within $\sim$10 ps when the pumping source is turned off. This carrier

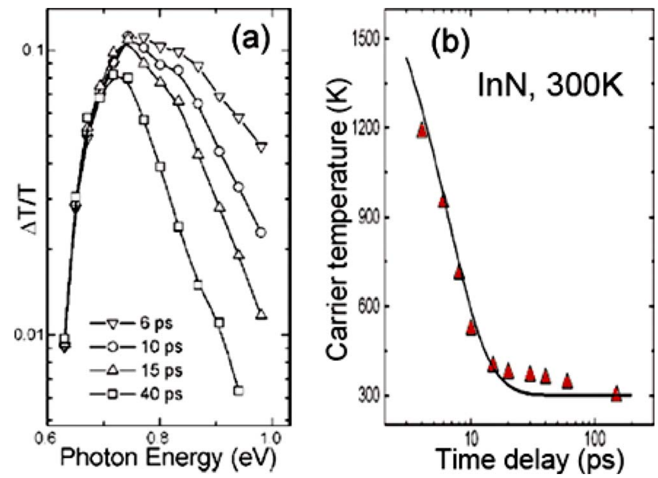

FIG. 17. (Color online) (a) Differential transmission spectrum at different time delays after the pump pulse is turned off. (b) Carrier temperature recorded at 300 K as a function of time delay calculated from (a). The solid curve is the expected behavior calculated using a LO phonon scattering model. Reference 93.

cooling is explained by a thermalization process involving carrier-LO phonon scattering,[93] as shown by the fitting curve in Fig. 17(b). More discussions on this process will be presented in Sec. III C.

III. InGaN AND InAlN ALLOYS

A. Bandgap and band alignment

1. Bowing of bandgap and critical point energies

The re-evaluation of the bandgap of InN brings new insights on studies of group III-nitride alloys that were already intensively investigated for their application in optoelectronics. Figure 18 shows the room-temperature absorption curves for In-rich InGaN (Ref. 92) and InAlN (Ref. 94) alloys over a wide range of compositions. As expected, the absorption edge shows a rapid blueshift from the bandgap of InN with increasing Ga or Al content.

The bandgaps of $In_{1-x}Ga_xN$ and $In_{1-x}Al_xN$ are plotted as a function of x in Fig. 19(a). Representative data on the Ga- or Al-rich side from literature are also shown for completion of the entire composition range.[95,96] As shown by the solid

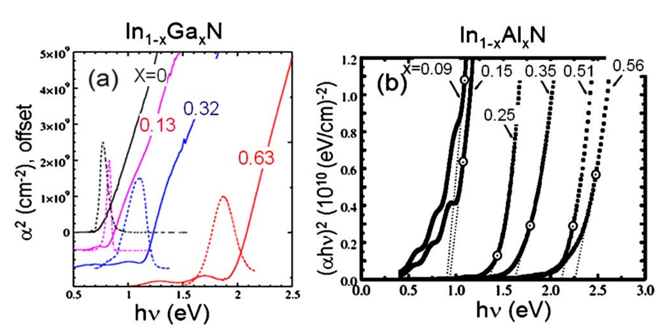

FIG. 18. (Color online) (a) Room-temperature PL spectrum (dashed) and absorption squared (solid) of InN and $In_{1-x}Ga_xN$ with different compositions. Ref. 92. (b) Room-temperature absorption curves of $In_{1-x}Al_xN$ alloys with different compositions, from which the bandgap is determined as a function of x. Reference 94.

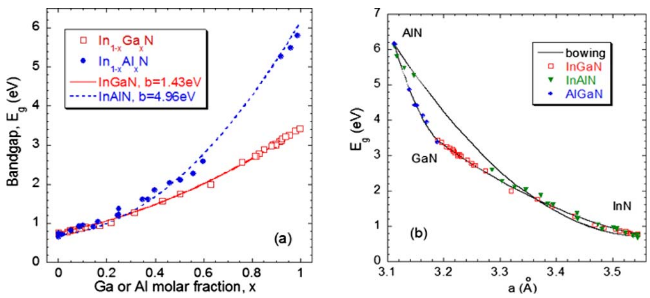

FIG. 19. (Color online) (a) Bandgap of InGaN and InAlN as a function of Ga or Al molar fraction. The solid and dashed lines are bowing curves [Eq. (13)] with best-fit bowing parameters. (b) The bandgap of InGaN, InAlN, and AlGaN plotted as a function of in-plane lattice constant a. The solid lines show the bowing dependence using the best-fit bowing parameters determined from (a). References 92, 94, and 95.

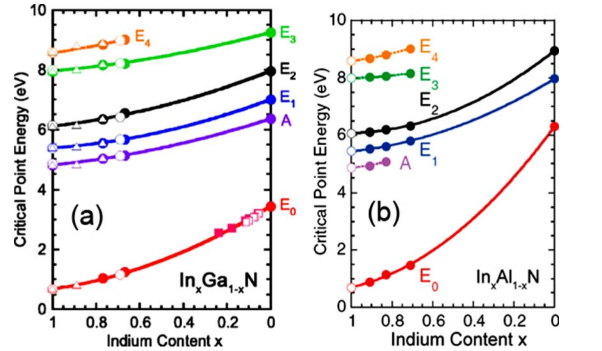

FIG. 20. (Color online) Bandgap and critical point energies of (a) InGaN (Ref. 45) and (b) InAlN (Ref. 43) as a function of the indium molar fraction. The solid lines represent the best fits using a bowing equation for determining the bowing parameters.

lines in Fig. 19(a), the bandgap of $In_{1-x}Ga_xN$ and $In_{1-x}Al_xN$ over the entire composition range can be well fit by the following standard bowing equation:

$$E_g(x) = E_g(0)\cdot(1-x) + E_g(1)\cdot x - b\cdot x\cdot(1-x). \qquad (13)$$

The bowing parameter is found to be $b = 1.4 \pm 0.1$ eV (Ref. 95) for $In_{1-x}Ga_xN$ and 5.0 ± 0.5 for $In_{1-x}Al_xN$.[94] The bowing for InGaN is relatively small, and agrees with most theoretical predictions.[40,97,98] A bowing parameter as large as 2.63 eV would be needed to explain the composition dependence of the bandgap on the Ga-rich side if an InN bandgap of 1.9 eV is assumed. Even when a narrow bandgap of InN was used, different experimental values of b equal to 2.5 eV,[99] 2.3 eV,[100] and 1.8 eV (Ref. 101) have been reported. As pointed out by Caetano *et al.*, it is critical to measure E_g over a large range of composition in order to have an accurate assessment of b.[98] Other effects such as strain, doping and composition fluctuation can also affect the measured bandgap bowing. On the other hand, the large b for $In_{1-x}Al_xN$ is related to its much wider bandgap range, and the large uncertainty of b comes from the more scattered data measured in this wide range of E_g. For discussion on the indirect bandgaps of group-III nitrides and their bowing, the readers are referred to Ref. 40.

It is inspiring to plot the bandgap bowing as a function of lattice constant instead of composition, so that the three alloys $In_{1-x}Ga_xN$, $In_{1-x}Al_xN$, and $Al_{1-x}Ga_xN$ can be plotted on the same coordinates. To do so, we assume a linear dependence of the lattice constant on composition following Vegard's law. The bandgap bowing in Fig. 19(a) is consequently mapped to a bowing as a function of in-plane lattice constant, as shown in Fig. 19(b). For the available range of experimental data, the bandgap of $In_{1-y}Al_yN$ falls practically onto the same curve of $In_{1-x}Ga_xN$. Therefore, In-rich $In_{1-x}Ga_xN$ and $In_{1-y}Al_yN$ will have the same bandgap if their compositions are tuned separately to match their lattice constant. The condition for such a concurrent lattice and bandgap match is $x \approx 1.25y$. It has been recently shown that the InGaN and InAlN alloys have good thermoelectric properties.[102,103] Even though $In_{1-x}Ga_xN$ and $In_{1-y}Al_yN$ have equal bandgaps at lattice-matched conditions, their acoustic properties such as thermal conductivity can be quite different.[102] If their CBM and VBM are shown to align well at this lattice-matched condition, superlattices of $In_{1-x}Ga_xN/In_{1-y}Al_yN$ would be an ideal electronically and lattice matched but acoustically mismatched system. Such systems can be of great interest in high-performance thermoelectrics.[104]

Similar to the bandgap, the high-energy critical points have also been measured as a function of composition for InAlN (Ref. 43) and InGaN (Ref. 45) using spectroscopic ellipsometry. The results are shown in Fig. 20. The bowing parameter for the energy of each of these critical points is determined by fitting with the bowing equation and listed in Table III. With this information, the complex dielectric function of the InGaN and InAlN alloys in the entire composition range can be parametrized with the standard analytical model.[107]

TABLE IV. Recommended values of basic physical parameters of zincblende InN, AlN, and GaN.

Parameter	AlN	GaN	InN
Lattice constant a (nm)	0.438[a]	0.450[a]	0.498[a]
Bandgap $E_g(T=0)$ (eV)	5.4[a]	3.3[a]	0.6[b]
Vashni parameter α (meV/K)		0.593[a]	
Vashni parameter β (K)		600[a]	
Electron effective mass m_e^*/m_0	0.32[c]	0.19[c]	0.05[c]
γ_1	1.45[c]	2.51[c]	6.82[c]
γ_2	0.35[c]	0.64[c]	2.81[c]
γ_3	0.60[c]	0.98[c]	3.12[c]
$m_{hh}^{[001]}/m_0$	1.33[c]	0.81[c]	0.84[c]
$m_{hh}^{[110]}/m_0$	2.63[c]	1.38[c]	1.37[c]
$m_{hh}^{[111]}/m_0$	3.91[c]	1.81[c]	1.74[c]
$m_{lh}^{[001]}/m_0$	0.47[c]	0.27[c]	0.08[c]
$m_{lh}^{[110]}/m_0$	0.40[c]	0.23[c]	0.08[c]
$m_{lh}^{[111]}/m_0$	0.38[c]	0.22[c]	0.08[c]
m_{so}/m_0	0.47[a]	0.29[a]	0.3[a]
Δ_{so} (meV)	19[a]	17[a]	5[a]
Volume deformation potential a_V (eV)	−10[c]	−7.3[c]	−3.8[c]
E_P (eV)	23.8[c]	16.9[c]	11.4[c]
TO phonon (1/cm)	655[d]	555[d]	472[d]
LO phonon (1/cm)	902[d]	742[d]	586[d]

[a]Reference 40.
[b]Reference 89.
[c]Reference 55.
[d]Reference 47.

2. Band alignment and offset

The band offset between group-III nitrides has been a focus of theoretical and experimental investigations long before the revision of the bandgap of InN. Because what is responsible for the revision is the conduction band-filling effect, previous studies of the valence band offset between InN and other nitrides are considered still valid. However, there is no consensus on the valence band offset between these materials owing to complications such as piezoelectric, strain, and spontaneous polarization effects.[40] Due to these effects the offset may be growth sequence dependent, i.e., different between the heterojunctions of *A* on *B* and *B* on *A*.[108] A wide range of values have been reported for the natural valence band offset between wurtzite InN and GaN. For example, on the calculation side, 0.3 eV,[109] 0.48 eV,[110] 0.7 eV,[111] and 1.27 eV,[112] and experimentally 0.5 eV,[113] 0.58 eV,[114] 0.78 eV,[115] 1.04 eV (In/Ga polar), or 0.54 eV (N polar),[108] 1.05 eV,[105] and 1.1 eV (Ref. 116) have been reported. We recommend the results of Martin *et al.* measured using x-ray photoemission spectroscopy,[105] because they systematically measured all three types of heterojunctions and reached self-consistent values. In their experiments the VBM of wurtzite InN was found to be ~1.1 eV above that of GaN (Ref. 105) after corrections to strain and piezoelectric effects. Therefore a type-I band alignment with $\Delta E_V/\Delta E_g=0.38$ exists in this system. This result and the GaN/AlN and InN/AlN band offsets are listed in Table III. The transitivity rule is clearly satisfied in these offset values. However, the readers are advised to take caution in using these values. Further development in the measurements of group III-nitride band offset is expected.

B. Electronic properties

1. Native defects and *n*-type doping

GaN is notoriously difficult to be doped *p* type. The doping disparity is even more pronounced for InN. As-grown InN has a strong propensity to be unintentionally *n* type, a behavior similar to GaN before better control of its growth and doping was achieved. The origin of the *n*-type conductivity in InN is still a topic of debate and investigation. First-principle calculations show that the nitrogen vacancy (V_N) is the lowest energy native defects, and can be a major source of free electrons in *n* type or compensating donors in *p*-type InN.[117–119] This view is supported by some experimental evidence.[26,120,121] Indium vacancy has also been found to play a role in the conductivity in InN.[122] Additionally, hydrogen in InN was predicted to act exclusively as a shallow single (when interstitial) or double (when substitutional) donor,[123] owing to the fact that H^0 and H^- are always higher in energy than H^+.[124] Experimental studies seem to support this prediction.[125–128] This is in contrast to the amphoteric behavior of hydrogen in GaN and AlN, where it is stable as a donor in *p* type and as an acceptor in *n*-type material, always compensating the prevailing conductivity.[129] Oxygen and silicon are expected to have a lower energy than V_N in *n*-type InN, therefore potentially a significant source of free electrons.[117,130] However, it was demonstrated by experiments combining Hall effect and secondary ion mass spectroscopy that O and H alone cannot fully account for the free electron concentration in unintentionally *n*-type InN.[65] Therefore native defects may play a critical role in the *n*-type unintentional doping. Besides point defects, edge-type threading dislocations[131] and V_N^+ segregated along dislocation lines[132] have been suggested to be a dominant source of free electrons in InN. Given the uncertainties with the source of background electrons in InN, more studies are needed before the *n*-type doping in In-rich InGaN can be fully understood.

2. *p*-type doping

p-type doping of InN and In-rich InGaN has been the focus of intense research efforts. Realization of their optoelectronic applications depends critically on the success of *p*-type doping. Mg is the most studied dopant acting as a possible acceptor in InN. Since evidence for *p*-type doping in InN was reported for the first time by Jones *et al.* in 2006,[133] many groups have confirmed and characterized hole conduction in Mg-doped InN.[134–140] Unlike undoped or *n*-type InN films, these films typically exhibit no or extremely weak photoluminescence at room temperature. Using low-temperature photoluminescence spectroscopy, Wang *et al.*[136] determined the acceptor ionization energy of Mg in InN to be about 61 meV, much shallower than 110 meV estimated by Anderson *et al.*,[134] but comparable to the acceptor binding energy of 50–55 meV reported by Klochikhim *et al.*[141] and 60 meV reported by Khan *et al.*[42] However, due to the background electron doping or surface electron accumulation (discussed below), all these Mg-doped InN films exhibit net *n*-type conductivity in direct Hall effect measurements. There seems to be a window of Mg concentration from $\sim 10^{18}$ to $\sim 3\times 10^{19}$ cm^{-3} that produces bulk *p*-type activity.[138] Outside this window, incorporation of Mg only partially compensates the background electron doping.[136] Miller *et al.*[142] observed the sign difference of thermopower between undoped and Mg-doped InN. Wang *et al.*[137] estimated the hole mobility to be 17–36 cm^2/V s. Using x-ray absorption fine-structure measurements, Miyajima *et al.*[143] determined that most of the Mg atoms occupy substitutional In sites. *p*-type activity in the bulk of In-rich $In_{1-x}Ga_xN$ alloys was also reported by Chang *et al.*[144] for In content up to 0.56 using Hall effect, King *et al.*[135] for $0<x<1$ using x-ray photoelectron spectroscopy, and Schaff *et al.* for $0<x<1$ using the hot probe method.[145] The binding energy of Mg acceptor was shown to decrease from GaN to InN.[144] A chemical trend is seen in the Mg acceptor binding energy from AlN to GaN (Ref. 41) and to InN, as listed in Table I.

3. Surface properties

Despite the clear evidence of free holes in the bulk, *p*-type conductivity has not been directly observed in Mg-doped InN by Hall effect. The reason is that the surface of InN is strongly electron accumulated regardless of the bulk doping, a direct consequence of the surface Fermi level being pinned deep in the conduction band.

The surface Fermi level pinning effect can be described by the amphoteric defect model developed by Walukiewicz.[146] In this model the states that pin the Fermi

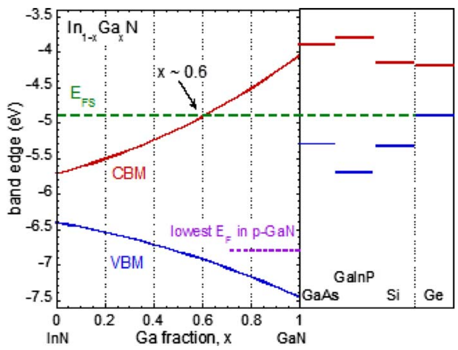

FIG. 21. (Color online) E_{FS} in InGaN alloys with respect to the natural conduction and valence band edges assuming no strain and polarization effects. The band edges of several other semiconductors are also shown. The energy is referenced to the vacuum level. Reference 67.

level (E_F) tend to fall near a universal energy level, known as the Fermi stabilization energy (E_{FS}). In compound semiconductors the formation energy of acceptor-type (donor-type) native defects, such as cation (anion) vacancies, decreases linearly as the Fermi level moves toward the conduction (valence) band. E_{FS} is defined as the crossover point of E_F when these two energies are equal. In the bulk, E_{FS} is the energy position where E_F tends to stabilize at by the creation of native defects that compensates the external doping. For the surface defect states associated with dangling bonds, surface reconstruction, contaminations, etc., the surface Fermi level tends toward E_{FS} to neutralize these states. E_{FS} lies ~4.9 eV below the vacuum level, and falls into the bandgap for most semiconductors. However, in InN and In-rich InGaN and InAlN, due to their exceptionally low CBM, E_{FS} is located deep in the conduction band, about 0.8 eV above the CBM, or ~1.5 eV above the VBM of InN as shown in Fig. 21 and Fig. 11(b). This energy configuration causes strong electron accumulation near the surface, hiding the *p*-type activity in the acceptor-doped bulk. Electrical properties, measured by Hall effect, are determined by electron transport in this surface layer rather than in the bulk of the sample. E_{FS} crosses the CBM of $In_{1-x}Ga_xN$ at approximately $x \approx 0.6$. Therefore, a surface electron accumulation is expected for In fraction exceeding ~0.4, while a surface depletion is expected for the rest of the composition. This effect has been experimentally confirmed by King *et al.* using x-ray photoemission spectroscopy.[147,148] They found that the transition from surface accumulation to depletion occurs at In fraction ~0.43 for *n*-type InGaN, and from surface inversion to hole depletion at In fraction ~0.59 for *p*-InGaN. A deviation of surface Fermi level pinning from E_{FS} was measured across the composition range. Similar surface electron accumulation was observed in InAlN alloys.[149] As shown in Fig. 11(b), a similar effect is expected in InAs as well, and indeed, a strong surface electron accumulation has been observed in InAs.[150]

The surface accumulation in InN was first suggested by Lu *et al.*[151] and Rickert *et al.*,[152] and directly probed by Mahboob *et al.* using high-resolution electron-energy-loss spectroscopy.[153,154] In the studies of Mahboob *et al.* the physics is described in terms of the branch-point energy (E_B) instead.[155,156] E_B is an energy level used to describe the pinning position of the Fermi level by defect states. These states

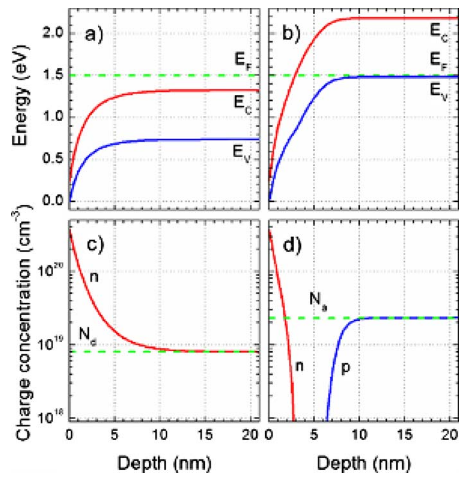

FIG. 22. (Color online) Band bending (a and b) and charge distribution (c and d) near the surface of a *n*-type (a and c) and *p*-type (b and d) InN film. The bulk doping level in each case is labeled by N_d and N_a, respectively. Reference 139.

are typically deep states that are spatially localized and therefore sample a substantial portion of the Brillouin zone, not just the band edges as hydrogenlike states do. The position of E_B in the band structure is determined by calculating the average midgap energy across the entire Brillouin zone,[155] as shown schematically in Fig. 13. E_B tends to coincide with E_{FS} because both are defined by deep defect states, regardless of their detailed nature and origin.

Given the surface Fermi level position, the band bending and charge distribution near the surface can be calculated by solving the Poisson equation numerically. Complications arise from the conduction band nonparabolicity,[20] band renormalization,[20] and quantum effects[154,157,158] at such high electron concentrations over a small depth. An example of the calculation is shown in Fig. 22, where the quantum confinement effect is neglected.[139] It can be seen that regardless of the bulk doping type and concentration, a surface electron accumulation (or inversion in the case of *p*-InN) exists with concentrations above 10^{20} cm^{-3} within a depth ~5 nm. Especially, for *p*-InN a *n*-*p* junction forms on the surface that prevents electrical contact with the bulk. The surface sheet electron concentration is as high as ~10^{13} cm^{-2}, the strongest native surface electron accumulation among any III-V semiconductor. Quantum confinement and quantized energy levels were observed in the surface layer by Colakerol *et al.* using angle-resolved photoemission spectroscopy, as shown in Fig. 23,[157] and quantitatively calculated by King *et al.*[159] The degree of band bending and sheet electron density can be also modulated by electrolyte gating as discussed below. Such a tunable two-dimensional electron gas naturally forming on the InN surface offers a simple system to probe interesting physics and explore new applications.

We note that the surface Fermi level pinning above the CBM in InN was explained by density functional theory calculations performed by Van de Walle *et al.*[160] The authors also predict an absence of such an electron accumulation on the nonpolar InN $(1\bar{1}00)$ and $(11\bar{2}0)$ surfaces, and on polar surfaces if processed to consist purely of In–N dimers. InN films with different polarities were first grown and studied by

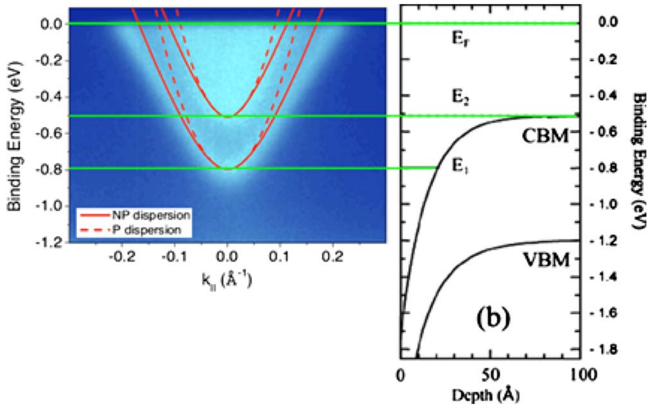

FIG. 23. (Color online) (a) Angle-resolved photoemission spectroscopy photocurrent intensity map of a n-type InN showing the quantized energy levels in the surface layer. Calculated subband dispersion shows clearly the band nonparabolicity (solid curves). (b) band diagram and energy levels. Refs. 157 and 159

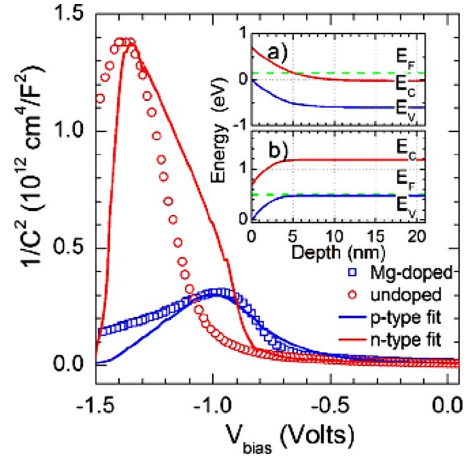

FIG. 24. (Color online) $1/C^2$ as a function of bias voltage determined by ECV measurements for unintentionally doped and Mg-doped InN along with two calculated curves for $N_d=8\times10^{18}$ cm^{-3} and $N_a=2.3\times10^{19}$ cm^{-3}. The inset shows the band bending configuration calculated for the unintentionally doped (a) and Mg-doped (b) films at their respective peak in the main plot. Ref. 139

Xu *et al.*[161] King *et al.* reported the universality of electron accumulation on both polar and nonpolar InN surfaces,[162] although Gwo *et al.* showed evidence of absence of accumulation layer on *in situ* cleaved nonpolar InN surfaces.[163]

Owing to the surface electron accumulation layer, direct Hall effect only measures the free carrier concentration averaged over the depth weighted by mobility. For nonuniform charge distributions such as these, capacitance-voltage (CV) profiling yields more information as it probes the net charge concentration as a function of depth. However, for InN the surface E_F is pinned above CBM, as such the required Schottky contacts for conventional CV profiling cannot be achieved with metals. Instead, a liquid electrolyte has been used to form a rectifying contact in a metal-insulator-semiconductor configuration, a technique known as electrochemical CV (ECV) profiling.[133] A bias voltage (V_{bias}) applied to the electrolyte with respect to the grounded sample bulk shifts the surface Fermi level to $E_F=E_{\text{FS}}+V_{\text{bias}}$. Thus a negative V_{bias} causes the surface energy bands to move upward relative to E_{FS}, making the surface bands bend less than in Figs. 22(a) and 22(b). At sufficiently large negative V_{bias}, a flat band, followed by surface depletion, and eventually inversion band configuration can be realized for both n- and p-doped films, provided that the electrolyte and film junction do not break down at these voltages. The capacitance (C) of the surface layer is monitored and plotted as a function of V_{bias}. Unlike the normal Mott–Schottky plot where $1/C^2$ is plotted against V_{bias} and the slope measures the doping level, in this situation a nonmonotonic behavior is seen on the $1/C^2$ versus V_{bias} plot. The peak corresponds to the V_{bias} when the surface E_F is displaced into the bandgap, such that the total space charge Q becomes desensitized to the variation of V_{bias}, because E_F is too far from both CBM and VBM to populate or depopulate the conduction or valence bands. For this V_{bias}, the system has the smallest $C=dQ/dV_{\text{bias}}$ and thus has a peak in $1/C^2$. The Mott–Schottky plot for a n- and a p-type InN film is depicted in Fig. 24, and compared to the theoretical curves and band configuration calculated by Yim *et al.*[139]

The peak height ($1/C^2$ at peak) is related to the bulk doping level (N_a or N_d), while the peak position (V_{bias} of peak) can be used to identify the bulk doping type. The latter is because the position of E_F at the peak relative to the surface CBM and VBM is not the same for n- and p-doped films. It is closer to VBM (CBM) on the surface for n (p)-doped InN, resulting in a peak at more negative V_{bias} for n-doped films than for p-doped ones. Namely, the surface E_F position where Q is the least sensitive to changes in V_{bias} is not exactly at the midgap; instead, it is pushed away from the doped band since Q would change rapidly at the onset of depletion of that band. This effect breaks the symmetry of the surface E_F in the bandgap, and quantitatively identifies the type of bulk doping by the position of the $1/C^2$ peak. As ECV is essentially the only technique for directly measuring the doping level in the presence of surface accumulation in narrow-gap semiconductors such as InN and InAs, this model provides a general guideline and calibration for analyzing doping in narrow-gap semiconductors. In Ref. 139 this model is also extended to InGaN alloys. Recent ECV experiments by Wang *et al.*[138] suggest that charges at surface states within the bandgap of InN also affect the capacitance, and a correction is needed to account for these states in ECV experiments. Brown *et al.* quantitatively probed the change in surface layer conduction using electrolyte-gated Hall effect.[164]

4. Radiation resistance

In view of the important role of native defects in the doping behavior of InN and InGaN, energetic-particle irradiation was used to systematically introduce point defects at controlled concentrations.[67] Radiation damage by different types of energetic particles can be calibrated using a single parameter known as the displacement damage dose (D_d).[165] Electrons, protons, and $^4He^+$ were used to produce a D_d spanning 5 decades. Most materials such as GaAs, GaInP, and GaN rapidly become electrically insulating with increasing D_d.[67,166] In stark contrast, the electrical conduction of

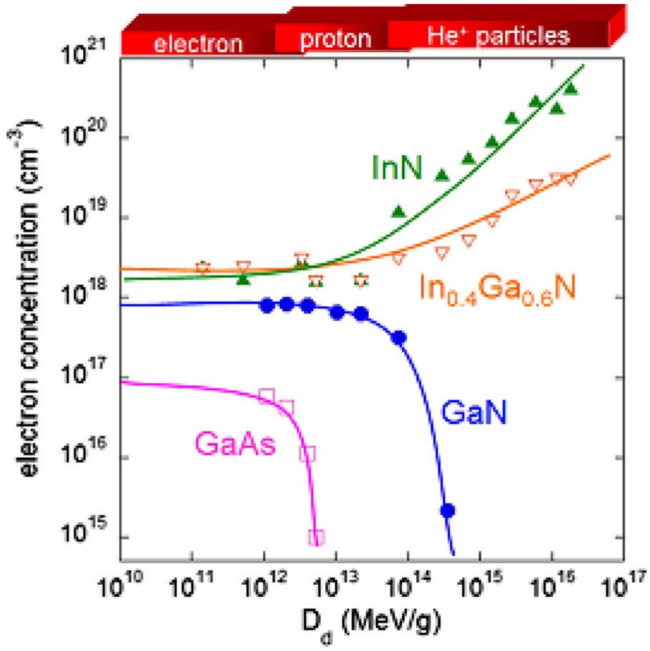

FIG. 25. (Color online) InN and InGaN alloys behave very differently from GaAs and GaN when irradiated with high-energy particles. Here the electron concentration is shown as a function of displacement damage dose. References 67 and 166

InN and In-rich InGaN does not deteriorate even at extraordinarily high doses of radiation. In fact, the free electron concentration increases with increasing radiation dose and saturates at sufficiently high doses, as shown in Fig. 25.[166] The saturation is consistent with the amphoteric defect model which predicts a final stabilization position of E_F at E_{FS}, above the CBM of InN and In-rich InGaN.[166] Positron annihilation spectroscopy measurements suggest that negatively charged N interstitials are generated at high rate by the irradiation, and may be the defects that ultimately limit the free electron concentration at high irradiation dose.[167] The electron mobility and minority carrier lifetime were also found to be much less sensitive to the irradiation than for GaAs and GaInP, which are the materials currently used in high-efficiency multijunction solar cells.[67] This superior radiation resistance of In-rich InGaN is desirable for device applications in radiative environments such as outer space and nuclear reactors.

5. Transport properties

The surface electron accumulation layer is expected to have different transport properties from the bulk, due to its high electron concentration, confined electron wave function in the out-of-plane direction, and its proximity to surface scattering centers. Using quantitative mobility spectrum analysis in variable magnetic field Hall measurements, the surface layer conduction has been deconvoluted from the bulk conduction assuming a two-layer conduction model. The surface layer and bulk mobility at room temperature for an InN film were found to be ~500 and ~3500 cm^2/V s, respectively.[168] Using this method for a Mg-doped InN film, a heavy-hole and light-hole conduction at distinctly different mobilities was separated from electron conduction which is

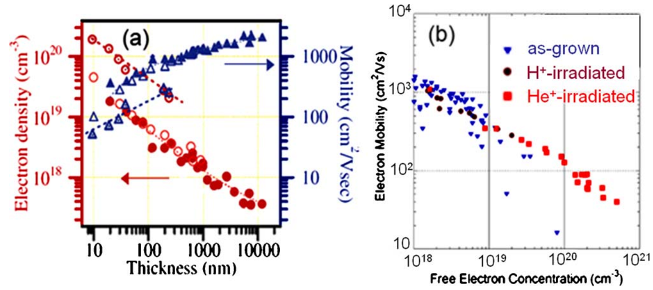

FIG. 26. (Color online) (a) As-grown InN electron density and mobility as a function of film thickness. Closed symbols are grown on a GaN buffer, open are on AlN buffer, and dotted symbols are grown directly on sapphire. Reference 145. (b) Electron mobility as a function of free electron concentration in as-grown InN films and films irradiated with 2 MeV H$^+$ or He$^+$ ions. References 176 and 177

attributed to the surface electron inversion layer.[134] Electric field dependence of the mobility of InN has been studied theoretically by Monte Carlo modeling, and a maximum mobility of 10 000 cm^2/V s (Ref. 169) and 14 000 cm^2/V s (Ref. 170) has been predicted for low carrier concentrations. Field-induced nonequilibrium electron distribution and transport in InN has been measured by Liang *et al.* and Tsen *et al.* using picosecond Raman spectroscopy, where a drift velocity as high as $(5\times10^7)\sim(2\times10^8)$ cm/s has been observed.[171,172] For a review on the comparison of high-field transport properties of group-III nitrides, see Ref. 173. We also note that Inushima *et al.* reported superconductivity[174] and Liang *et al.* reported large magnetoresistane in InN (Ref. 175) at low temperatures (<2 K).

For not intentionally doped InN, Hall effect always shows electron conduction, and the electron concentration and mobility are a strong function of film thickness. Figure 26(a) shows a summary given by Schaff *et al.*[145] It was pointed out that the electron concentration follows defect density caused by lattice mismatch, which decreases for thicker films. Therefore, native defects, not impurities, and contaminations, are the prominent electron sources in these films.[145,176] A strong correlation between the electron mobility and concentration was observed in as-grown InN, as shown in Fig. 26(b). The energetic-particle irradiated samples also approximately follow the same dependence, motivating the use of irradiation for a controlled study of the behavior of native defects in InN and its alloys.[176,177]

Using a variational procedure, Hsu *et al.* calculated various electron scattering mechanisms in InN and its alloys.[178] By fitting their calculated results to experimental mobility data, they conclude that in pure InN, Coulomb scattering from charged centers is the dominant mobility-limiting mechanism, although scattering from polar optical phonons and piezoelectric mode acoustic phonons becomes important at low doping concentrations ($<\sim10^{18}$ cm^{-3}) and at high temperatures (>400 K). In InGaN and InAlN, Coulomb and alloy disorder scattering are the dominant processes, as shown in Fig. 27. The defects resulting from irradiation of InN and its alloys are found to be triply charged donors. Using Monte Carlo simulations, Yu *et al.* modeled the effects of dislocations on electron transport in InN.[179] They con-

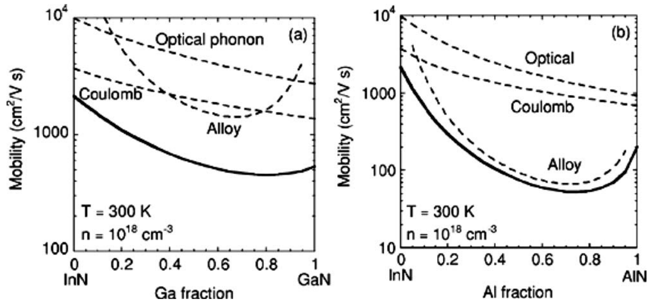

FIG. 27. Calculated electron mobility as a function of alloy composition in (a) InGaN and (b) InAlN. Main scattering mechanisms limiting the mobility are shown. References 178.

cluded that at high dislocation densities or low electric fields the mobility of electrons is strongly affected by the dislocations.

C. Pressure behavior and lattice properties

1. Hydrostatic pressure coefficient and deformation potentials

It is intriguing to note that the bandgaps of InGaN and InAlN are approximately a single function of their lattice constants, which suggests that the atom size effect is very important in determining the bandgaps. An effective experimental means to decouple the chemical influence from the atomic size effect on the bandgap is by application of hydrostatic pressure.

There have been a few experimental studies on the pressure behavior of GaN,[180,181] Ga-rich InGaN alloys[180,182] and AlN.[60] Although there is a relatively good consensus on the bandgap pressure coefficients of GaN and AlN, much less has been known about the pressure dependence of the energy gaps in In containing group III-nitride alloys. A wide range of bandgap pressure coefficients has been found even in the most extensively studied Ga-rich InGaN alloys.

The pressure coefficients of the bandgaps (dE_g/dP) of InN and In-rich InGaN and InAlN alloys in comparison with those of AlN and GaN are shown in Fig. 28. dE_g/dP of InN has been measured to be 2.7,[62] 2.8,[61] or 3.0 meV/kbar,[63]

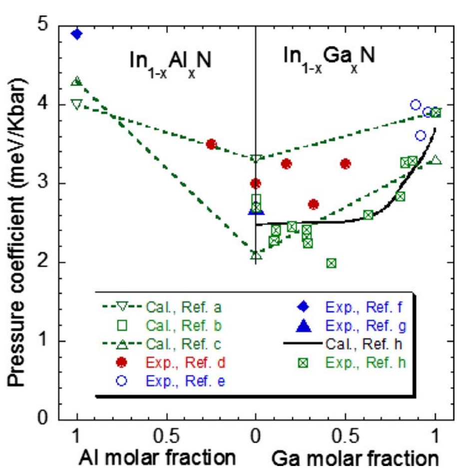

FIG. 28. (Color online) Hydrostatic pressure coefficients of the bandgaps of InN, GaN, AlN, and their alloys. Refs: a 59, b 183, c 58, d 63, e 180, f 60, g 62, h 61.

close to the theoretical value predicted by Bellaiche *et al.*[183] For InGaN alloys the pressure coefficient is in between the two theoretical predictions by Wei and Zunger[58] and Christensen and Gorczyca.[59] Considering the pressure coefficient of GaN to be ~4 meV/kbar,[180] it is interesting to see how dE_g/dP of InGaN increases from InN to GaN. Recently Franssen *et al.* presented experimental and theoretical results showing that dE_g/dP has a nonlinear dependence on the Ga fraction, as shown in Fig. 28.[61]

dE_g/dP of $In_{0.75}Al_{0.25}N$ was measured to be ~3.5 meV/kbar, and extrapolates to a value of ~5 meV/kbar at $x=1$; this agrees well with the pressure coefficient of AlN determined from absorption experiments.[60] Note that the pressure coefficients of the group-III nitrides are much smaller than those of other III-V compounds. For example, $dE_g/dP=11$ meV/kbar for GaAs (Ref. 184) is almost three times larger than that for GaN. This trend can be attributed to the larger ionicity of the group-III nitrides due to the high electronegativity of N. In group III-V semiconductors, higher ionicity typically leads to smaller pressure coefficients.[185] The Phillips ionicity is 0.31 for GaAs and is significantly smaller than 0.50 for GaN. The trend applies to group-III nitrides as well, among which larger cations give higher ionicity [AlN $f_i=0.449$, GaN $f_i=0.500$, and InN $f_i=0.578$ (Ref. 36)] and thus smaller pressure coefficients.

The volume deformation potential of the bandgap ($a_V=dE_g/d\ln V$) in group-III nitrides has been calculated by various groups. These calculations generally give good agreements, such as $a_V=-4.1,-7.8,-8.8$ eV,[59] −3.7, −7.4, and −10.2 eV,[58] −3.1, −7.7, and −9.8 eV,[186] and −4.2, −7.6, and −9.8 eV (Ref. 55) for InN, GaN, and AlN, respectively. The decrease in $|a_V|$ with increasing ionicity is evident.[58] The bulk modulus ($B=-dP/d\ln V$) has been theoretically calculated as well. Experimental results of B scatter within a wide range between 1260–1480 kbar for InN,[32] 1880–2450 kbar for GaN,[187,188] and 1850–2079 kbar for AlN.[189–191] In Table III we recommend Wei and Zunger's results as they calculated both a_V and B systematically.[58]

2. Piezoelectric properties

The lack of center of symmetry in group-III nitrides results in piezoelectricity. They also exhibit spontaneous polarization with polarity determined by the terminating anion or cation plane on the surface. A review of the piezoelectric coefficients d_{13}, d_{33}, and d_{15} and polarization P_{sp} was presented in Ref. 40. As the bandgap revision is not expected to affect these properties, we recommend the same values as recommended in Ref. 40 and list them in Table III. As a result of the piezoelectric and spontaneous polarization effects, a two-dimensional electron gas is expected to form on the interface of InN with InGaAlN alloys. Modeling of transport properties of such structures was performed by Hasan *et al.*,[192] Kong *et al.*,[193] and Yarar *et al.*[194]

3. Phonon structures and dynamics

For the wurtzite structure, group theory predicts eight sets of normal phonon modes at the Γ point, $\Gamma_{acoustic}$

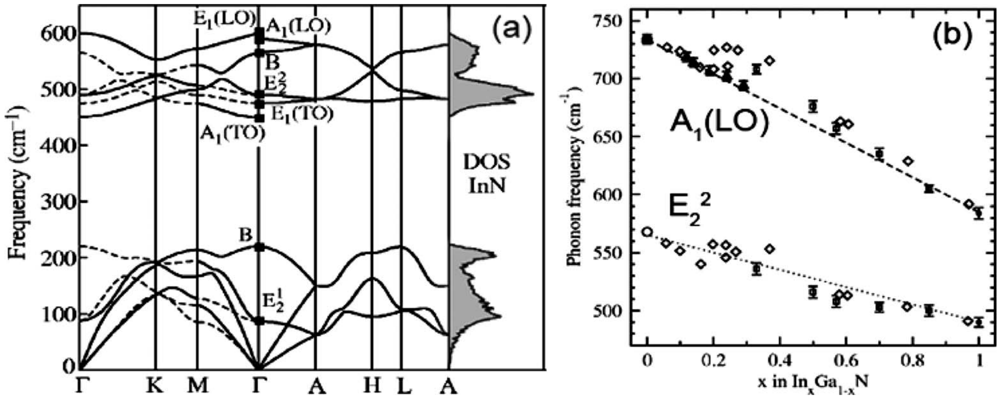

FIG. 29. (a) Calculated phonon dispersion and density of states in wurtzite InN. Ref. 48 (b) Composition dependence of the E_2 and A_1(LO) modes in $In_xGa_{1-x}N$ alloys. References 196 and 197.

$+\Gamma_{\mathrm{optical}}=(A_1+E_1)+(A_1+2B_1+E_1+2E_2)$. The atomic displacement scheme of these phonon modes is depicted in Ref. 47. Among the six optical phonons, the two E_2 modes are only Raman active, the A_1 and E_1 modes are both Raman and IR active, and the two B_1 modes are neither Raman nor IR active (silent). For wurtzite film grown on (0001) substrate, only the E_2 and A_1(LO) modes are allowed by the polarization selection rules in backscattering geometry.[195] This results in the fact that the E_2^2 and A_1(LO) modes are the best studied phonon modes in group-III nitrides. Figure 29(a) shows the phonon dispersion of wurtzite InN and the corresponding phonon density of states calculated by Davydov *et al.*[48] The E_2 and A_1(LO) modes in InGaN alloys measured by Raman scattering spectroscopy have a linear dependence on the composition, as shown in Fig. 29(b) which contains experimental data measured by several groups.[196,197] The phonon modes in InAlN alloys have not been thoroughly experimentally characterized. However, from the linear composition dependence of A_1(LO) and E_2 phonon energies in InGaN alloys, it is reasonable to assume that the phonon energies also interpolate linearly between InN and AlN. There is little controversy in the phonon energies in InN, GaN, and AlN. Recommended values are listed in Table I.

From Fig. 29(a) it can be seen that there exists a large phononic bandgap in InN. This is understandable given the fact that the atomic mass of In differs from that of N by a factor of 8.2. A simple diatomic linear chain model (with heavy atomic mass M and light atomic mass m) predicts a relative phononic bandgap of[198]

$$\frac{\omega_{\mathrm{optical}}^{\mathrm{min}}-\omega_{\mathrm{acoustic}}^{\mathrm{max}}}{\omega_{\mathrm{acoustic}}^{\mathrm{max}}}=\sqrt{\frac{M}{m}}-1, \tag{14a}$$

and a relative optical phonon band width of

$$\frac{\omega_{\mathrm{optical}}^{\mathrm{max}}-\omega_{\mathrm{optical}}^{\mathrm{min}}}{\omega_{\mathrm{optical}}^{\mathrm{min}}}=\sqrt{1+\frac{m}{M}}-1. \tag{14b}$$

Although this model overestimates the phononic bandgap and underestimates the phonon band width, the trend with m/M is clear. InN is thus expected to have the widest phononic bandgap and the narrowest optical phonon band width among all group III-V semiconductors.

Such a wide phononic bandgap and narrow phonon band width present interesting opportunities for applications in hot-carrier solar cells. In such cells the thermalization of photoexcited carriers is slowed down to allow time for the carriers to be extracted while they are still "hot," and thus achieving a high photovoltage.[199] Hot carriers lose their energy by emitting optical phonons. The optical phonons then decay predominantly by two mechanisms: the Klemens process, where an optical phonon decays into two LA phonons with opposite momentum and energy of half that of the optical phonon;[200] the Ridley process, where a LO phonon decays into a TO phonon and a LA phonon.[201] In materials with large phononic bandgap between optical and acoustic phonons, the Klemens process is blocked; in materials with narrow optical phonon band width, the Ridley process is less likely. InN has a phonon structure that well fits these conditions. Therefore, hot carriers are expected to have a long lifetime in InN due to its beneficial phonon structure, a phenomenon known as the phonon bottleneck effect. In fact cubic InN is expected to be an even better choice as a hot-carrier absorber.[202]

A relatively long hot-carrier lifetime has been reported in InN by Chen *et al.* as shown in Fig. 17(b).[93] Zanato *et al.*[203] and Pacebutas *et al.*[204] reported electron-phonon scattering time and optical bleaching effects in InN, respectively, both agreeing with a long hot-carrier lifetime. However, Sun *et al.* recently reported a shorter hot-carrier lifetime of ~0.4 ps,[205] and the same group argued that the plasma screening of electron-LO phonon interactions, rather than the hot phonon effect, is responsible for the slow energy loss rate.[206] Optical phonon lifetimes on the order of approximately picoseconds have also been observed by Pomeroy *et al.* using Raman scattering spectroscopy.[207] Ascazubi *et al.* reported that the hot-carrier thermalization was significantly accelerated when InN is doped with Si,[91] an effect the authors attribute to Si-induced electronic states in the electronic bandgap; however, Conibeer *et al.* point out that a more likely explanation would be that Si introduces vibrational states into the phononic bandgap, and hence facilitates the Klemens mechanism.[202] The possible slow hot-carrier thermalization combined with the tunable bandgap of In-rich InGaN alloys motivates studies for applications in high-efficiency solar cells.

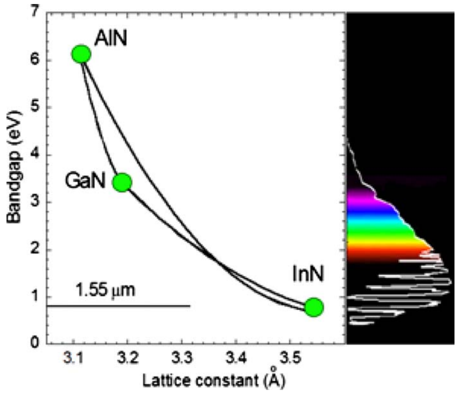

FIG. 30. (Color online) The bandgap of the group III-nitride alloys as a function of the *a*-axis lattice constant, compared to the visible colors, solar spectrum, and 1.55 μm wavelength.

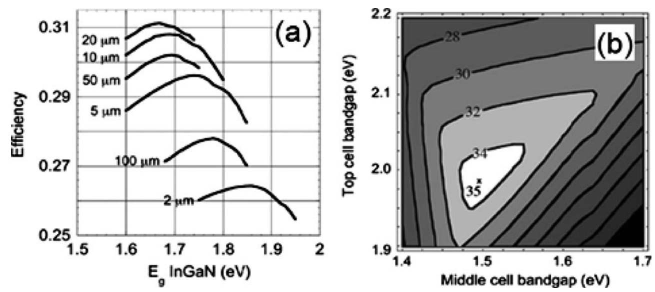

FIG. 31. (a) Calculated efficiency of high-quality InGaN/Si two junction solar cells as a function of InGaN bandgap. The physical thickness of the Si junction is labeled for each curve. (b) Isoefficiency plot of an $In_{1-x}Ga_xN/In_{1-y}Ga_yN/Si$ triple-junction solar cell as a function of the bandgaps of the two InGaN junctions. Reference 211.

IV. NEW APPLICATIONS

The re-evaluation of the InN bandgap and subsequent findings have a significant impact on device applications of group-III nitrides. The bandgap of InGaN alloys ranging from 0.64 to 3.42 eV provides an almost perfect match to the solar spectrum, as shown in Fig. 30. This opens up an interesting opportunity for using these alloys in high-efficiency solar cells. The important wavelength 1.55 μm for fiber optics is just slightly higher in energy than the bandgap of InN, and therefore can be emitted by InN when alloyed with small fractions of GaN, stressed, quantum confined, or doped with high electron concentrations. The visible spectrum is well within the bandgap range of the InGaN alloys, offering a possibility to fabricate full-color light emitting devices with this single alloy system. The surface electron accumulation layer and small effective electron mass of InN also find applications in chemical sensing and fast electronics. In the following we summarize the state-of-the-art developments in these applications.

A. Photovoltaics

InN and InGaN have the following advantages for solar cell applications: (i) bandgap continuously tunable within the energy range of the solar spectrum; (ii) superior resistance against high-energy particle radiation, making them especially suitable for space applications; (iii) possible strong phonon bottleneck effect to slow down hot-carrier cooling; (iv) advantageous band alignment with respect to Si, so that a recombination junction naturally exists for cells using a Si base. Since it was first proposed to use InGaN for solar cell applications,[67] significant efforts and progress have been made toward this goal, while great opportunities and grand challenges coexist.

The maximum solar energy conversion efficiency ($\sim$43%) is achieved in triple-junction cells based on three different semiconductors with fixed bandgaps and nearly matched lattice constant, Ge (0.7 eV), GaAs (1.4 eV), and GaInP (1.9 eV). In order to attain >50% conversion efficiencies using the multijunction concept, four or a greater number of junctions are needed. Finding materials with the required bandgap becomes a major challenge. For example, from detailed balance modeling, for an ideal four-junction solar cell that can reach 62% theoretical efficiency, a tandem of junctions with bandgaps of 0.6, 1.11, 1.69, and 2.48 eV is required.[208] The InGaN alloys would allow fine tuning in optimization of the performance of these cells by offering flexibility in the choice of the bandgaps.[209]

For double-junction cells, the maximum theoretical efficiency is about 39% when two junctions with bandgaps of 1.1 and 1.75 eV are used.[210] Silicon has a bandgap of 1.1 eV, ideally suitable for the bottom junction. $In_{1-x}Ga_xN$ has a bandgap of 1.75 eV when $x \sim 0.5$. Therefore, a tandem structure of p-$In_{0.5}Ga_{0.5}N/n$-$In_{0.5}Ga_{0.5}N/p$-Si/n-Si would form a high-efficiency double-junction cell. An additional benefit of this structure comes from the band alignment between InGaN and Si.[211] As shown in Fig. 21, at $x \sim 0.5$, the VBM of Si lines up with the CBM of $In_{1-x}Ga_xN$. Therefore, the n-$In_{0.5}Ga_{0.5}N/p$-Si interface would be a low-resistance Ohmic junction, acting as a natural "recombination junction" connecting the top and bottom cells. Heavy doping of the interface that is normally required for multijunction cells is not necessary in this cell. Using an analytical model developed by Kurtz *et al.*,[210] Hsu and Walukiewicz calculated[211] the theoretical efficiency of such a double-junction cell. They found that double-junction InGaN/Si solar cells can have significantly higher efficiencies than single-junction Si solar cells, with energy conversion efficiencies of more than 31% when high-quality materials are used [Fig. 31(a)]. For low-quality polycrystalline Si, adding an InGaN junction on top of Si can increases the efficiency by more than 50%, from 17% for Si alone to 27%. Such an increase in the efficiency could justify the cost increase associated with the complexity of growing these cells. Adding a second InGaN junction with an appropriate composition can provide further boosts to the efficiency. A three-junction $In_{1-x}Ga_xN/In_{1-y}Ga_yN/Si$ solar cell could offer energy conversion efficiencies exceeding 35% [Fig. 31(b)].

Besides integrating on a Si junction to form a multijunction cell, InGaN can also be used for a single-junction solar cell that meets the 2.4 eV requirement in a lateral cell architecture.[212,213] In this design, solar cell arrays with different bandgaps are laid out laterally; the sunlight is dispersed by optics and focused separately onto these solar cells that best match the wavelengths, so that over 90% of the photons will land on the correct solar cells and maximize the

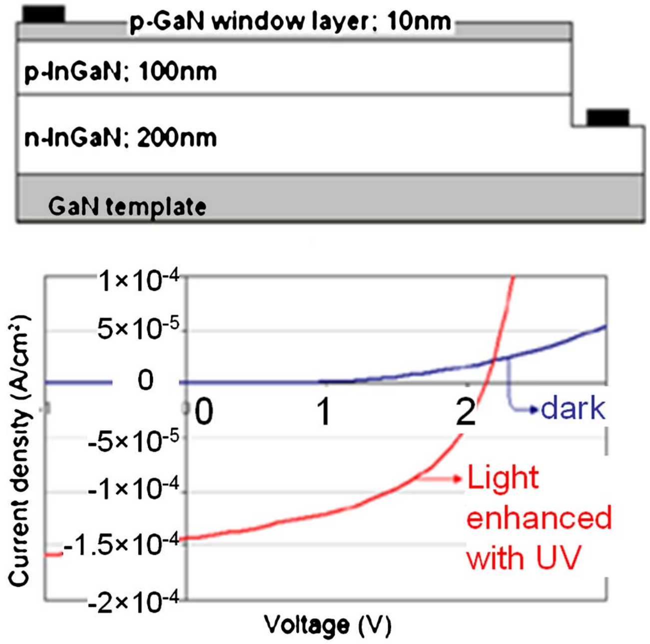

FIG. 32. (Color online) *I-V* characteristic of an $In_{0.28}Ga_{0.72}N$ solar cell under dark and UV-enhanced illuminated conditions. The device structure is schematically shown on the top. Reference 229.

total energy conversion. In addition, other exotic concepts such as graded-bandgap solar cells[214] can also be explored with the InGaN system. We note that growth of graded-composition InGaN thin films has been demonstrated.[215]

Fabrication of these cells faces major challenges, including lattice mismatch, *p*-type doping, phase separation, and surface states. $In_{1-x}Ga_xN$ (0001) has a lattice mismatch with Si (111) between 8% (when $x=0$) and 16% (when $x=1$). InN films[216–222] and nanowire arrays[218,223,224] have been grown epitaxially on Si substrates using MBE or MOCVD.[225–227] In order to achieve good film quality, a thin Si_3N_4 or AlN layer is typically used as a buffer. However, it is not clear whether these structures currently have materials quality suitable for high-performance photovoltaics. Similar issues need to be addressed in the $In_{1-x}Ga_xN/In_{1-y}Ga_yN$ cell and graded-bandgap cell. *p*-type doping of InN and In-rich InGaN is still in the exploratory stage, and a *p-n* junction has yet to be demonstrated. Nevertheless, fabrication of Ga-rich InGaN cells has been attempted by several groups.[228–231] Figure 32 shows the structure and performance of a single-junction $In_{0.28}Ga_{0.72}N$ solar cell grown by Jani *et al.* using MOCVD.[229] The high open-circuit voltage of 2.1 eV is consistent with the bandgap of $In_{0.28}Ga_{0.72}N$ at 2.4 eV. This is the highest In composition in a *p-n* junction that has been reported to show a strong photovoltaic response. Further increase in In composition leads to leaky junctions with poor photovoltaic performance as shown by Chen *et al.*[230] Phase separation in InGaN is detrimental to the device performance because it reduces the short-circuit current by generating recombination centers, and reduces the open-circuit voltage through bandgap fluctuations. In the work of Jani *et al.*, the phase separation was controlled by increasing the indium carrier gas flow rate, increasing the growth rate and limiting the thickness of the epitaxy.[229] The same group also reported the fabrication of *p*-GaN/*i*-InGaN/*n*-GaN solar cells which show high open-circuit voltage and high internal quantum efficiency.[232] Surface states in InN and In-rich InGaN tend to accumulate a high density of electrons over the depth of several nanometers from the surface, regardless of the bulk doping type (see Sec. III B). This surface electron layer prevents a direct Ohmic contact to *p*-type InGaN. No evidence has been shown that such a surface inversion layer on In-rich *p*-InGaN can be removed by passivating the surface states. Alternatively, it is possible to grade the composition of InGaN toward the surface, such that the surface composition becomes Ga-rich, making an Ohmic contact possible. However, the grading scheme has to be carefully designed so as not to block the majority carrier flow.

B. Solid state lighting and 1.55 μm and terahertz emission

The EQE of LEDs based on Ga-rich InGaN drops at the green wavelengths, which are, ironically, at the peak of the human eye response and a critical component of natural white lighting [Fig. 1(b)]. As a result, efficient full-visible-spectrum LEDs using a single materials system are not available. Solid state white lighting is currently achieved in a relatively inefficient way by combining blue InGaN LEDs with phosphor technology. Realizing high-EQE green and even red LEDs with InGaN is recognized as one of the major research challenges for solid state lighting.[5] The inefficiency of green emission in InGaN is believed to arise from multiple effects. This includes spinodal decomposition of InGaN at high In contents, the piezoelectricity-induced quantum-confined Stark effect that spatially separates the electron and hole wave functions, and nonradiative recombination associated with native defects.[233]

Bright PL has been achieved in InGaN films over the entire spectral range from the bandgap of InN to that of GaN,[61] as shown in Fig. 33(a). However, electrically driven InGaN light emitting devices require the formation of either a *p-n* junction of InGaN, or *p-i-n* quantum wells where InGaN is the active *i* region and GaN is typically used as the barrier. The first approach faces the same obstacles as in solar cell applications, namely, *p*-type doping and Ohmic contacts. The second approach is challenged by the incompatibility of growth temperatures of InGaN and GaN layers, as InGaN tends to decompose at temperatures that are still too low to grow high-quality GaN. Nonetheless, recent advances in thin film deposition techniques enable the growth of InGaN-based multiple quantum well (MQW) LEDs with ever increasing In content. Figure 33(b) shows the emission spectra of $In_xGa_{1-x}N/GaN$ MQW LEDs fabricated by Xu *et al.* using plasma-assisted MBE.[234] The In fraction is 0.18, 0.41, and 0.46 for the blue, green, and red emitting devices, respectively. Green and longer-wavelength LEDs with similar structure based on InGaN have been reported by several groups.[233,236–239] White LEDs based on multiple-color emission from InGaN LEDs have also been demonstrated.[240,241] In these works the In fraction incorporated in InGaN is still less than but close to 0.5. With these rapid developments, there are plenty of reasons to believe that the "green valley

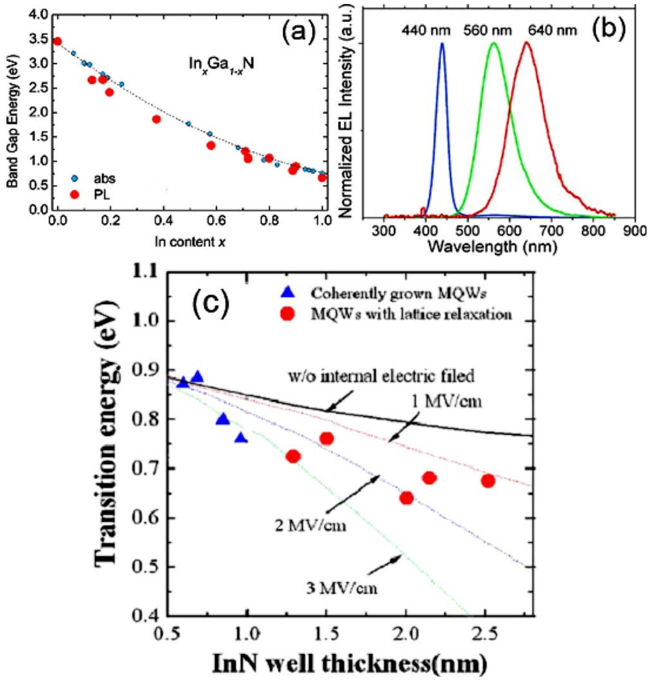

FIG. 33. (Color online) (a) Photoluminescence peak energy of $In_xGa_{1-x}N$ films with composition covering the entire range $0<x<1$. Refs. 61 and 95. (b) Electroluminescence spectra of $In_xGa_{1-x}N/GaN$ MQW LEDs. The In fraction is 0.18, 0.41, and 0.46 for the blue, green and red emitting devices, respectively. Reference 234. (c) $InN/In_{0.7}Ga_{0.3}N$ MQWs with different InN well widths emitting near 1.55 μm. Calculated dependence assuming different internal electric field is also shown. Reference 235.

of death" in solid state lighting will soon be overcome, and InGaN solid state lighting will be extended into the entire visible-IR spectrum.

1.55 μm (0.8 eV) light emission can be readily achieved by quantum confining InN or alloying with GaN. Figure 33(c) shows the PL peak energy of $InN/In_{0.7}Ga_{0.3}N$ MQWs with different InN well thickness reported by Che *et al.*[235] The same group also proposed and demonstrated InN/GaN MQWs consisting of 1 ML or few-monolayer InN wells inserted in a GaN matrix.[242] It was found that such MQWs have high structural and optical quality due to the self-ordering effect between InN and GaN. This approach may allow multiple InGaN layers with drastically different compositions to be grown at similar temperatures. In such structures excitons will be strongly localized in the low-band-gap region, possibly leading to room-temperature excitonic devices and wide-spectrum emitters. A similar approach has been taken by Dimakis *et al.* to produce near-UV LEDs.[243]

The quest for brighter sources in terahertz spectroscopy and imaging has also placed InN into the focus of investigation for terahertz emission. The first demonstration of strong terahertz emission from narrow-gap InN was reported by Ascazubi *et al.*,[244] where the emission was attributed to optically excited transient photocurrents. Later Matthaeus *et al.* compared the terahertz emission of InN with other semiconductors and concluded that the emission mechanism is the photo-Dember effect that occurs as a result of different diffusion coefficients of electrons and holes.[245] Mu *et al.* attributed the terahertz emission in InN to resonance-enhanced optical rectification.[246] Comparing InN and InAs, Polyakov and Schwierz[247] analyzed the importance of band structure in the terahertz emission efficiency. Very recently, Ahn *et al.* reported a significant enhancement in terahertz emission power from *a*-plane InN films, and explained the effect by the acceleration of photoexcited carriers under the polarization-induced in-plane electric field.[248]

C. Chemical sensors and field-effect transistors

The unusual band bending and electron accumulation near the surface of InN are being exploited for chemical sensing and field-effect devices. Soon after the discovery of the narrow bandgap of InN, Lu *et al.* reported a fast response of sheet carrier concentration and mobility to solvent exposures such as methanol and water.[249] Pt-coated InN nanorods were found to change resistance upon exposure to H_2 but not to N_2 and O_2.[250] The InN surface has been functionalized by aminosilane molecules and used to bind negatively charged Au colloids.[251] Anion sensing using InN with remarkable selectivity, stability, response time, and repeatability was shown by Lu *et al.*[252,253] In these experiments InN is sensitive to anions but not cations, indicating that the sensing mechanism is based on positively charged surface states of InN attracting negatively charged ions in aqueous solutions.

High electron drift velocities in InN were reported by Tsen *et al.* using ultrafast Raman spectroscopy.[172] The cutoff drift velocity at $\sim 2\times 10^8$ cm/s is higher than that of other group III-V semiconductors. This is understood by the band structure of InN featuring a low electron effective mass at the Γ point and a large energy separation between the Γ point and satellite valleys. In light of these superior properties, Lin *et al.* fabricated the first field-effect transistors (FETs) based on InN/AlN heterojunctions.[254] A standard transistor behavior was observed with a high source-drain current density that was attributed to the high sheet carrier density in such a ultrathin InN layer. Hauguth-Frank *et al.* fabricated photodetectors using ultrathin $In_{1-x}Ga_xN$ ($x<0.44$) layers.[255] Lebedev reported that in ultrathin $In_{1-x}Ga_xN/GaN$ ($x<0.5$) heterostructures, free electrons tend to accumulate at the buried InGaN/GaN interface instead of on the surface, and therefore the mobility is limited by the interface quality.[256]

V. GROUP III-NITRIDE NANOSTRUCTURES

In recent years, semiconductor nanostructures have come under extensive investigations for applications in high-performance electronic[257,258] and optical[259] devices. They offer a distinct way to study electrical, photonic, and thermal transport phenomena as a function of dimensionality, size reduction, and surface-to-volume ratio. In particular, a wide range of demonstrated and potential applications have made semiconductor nanowires (NWs) and quantum dots (QDs) a rapidly growing focus of research. With the interesting properties of InN and In-rich group-III nitrides described in previous sections, there has been much exploration into the growth and characterization of InN, $In_{1-x}Ga_xN$, and $In_{1-x}Al_xN$ nanostructures.

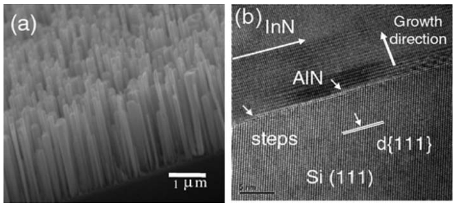

FIG. 34. (a) InN nanowire arrays grown on Si substrate by MBE. (b) The epitaxial interface between the InN nanowire and Si where an AlN buffer layer was used. Reference 260.

A. InN nanostructures: Optical properties

InN NWs have been grown using low-temperature MBE and MOCVD. Figure 34 shows such an example. These InN NW arrays were grown epitaxially on Si (111) substrates by Calleja *et al.* using plasma-enhanced MBE.[260] Under N-rich growth conditions InN tends to form such single-crystal NW arrays. Growth of InN nanostructures with various geometries, such as nanowires,[261–268] nanorods,[224,269,270] nanocolumns,[217,224,260,271] nanotips,[272,273] nanotubes,[274] nanobelts,[275,276] and nanocrystals,[277–279] has been reported by numerous groups. Most of these studies showed a light emission consistent with the narrow bandgap near 0.7 eV.

Figure 35(a) shows the bandgap and PL intensity of InN NWs as a function of electron concentration (n) derived from fitting the PL line shape with a model that considers the electron and hole distributions in the nanowires.[266] The PL intensity was found to scale as $\sim n^{-2.6}$, a stronger dependence than that of the Auger recombination, for which a dependence of n^{-1} is expected. The authors thus conclude that the decrease in PL efficiency arises not only as a result of the increase in bulk electron concentration, but also because of increasing importance of nonradiative recombination processes, such as recombination at the nanowire surface possibly related to the intrinsic surface accumulation layer. The fundamental bandgap is reduced in this layer, an evidence of the bandgap renormalization effect.[20] In nanowires these effects become more prominent due to the large surface-to-volume ratio. They are responsible for the decrease in E_g with increasing n in Fig. 35(a).

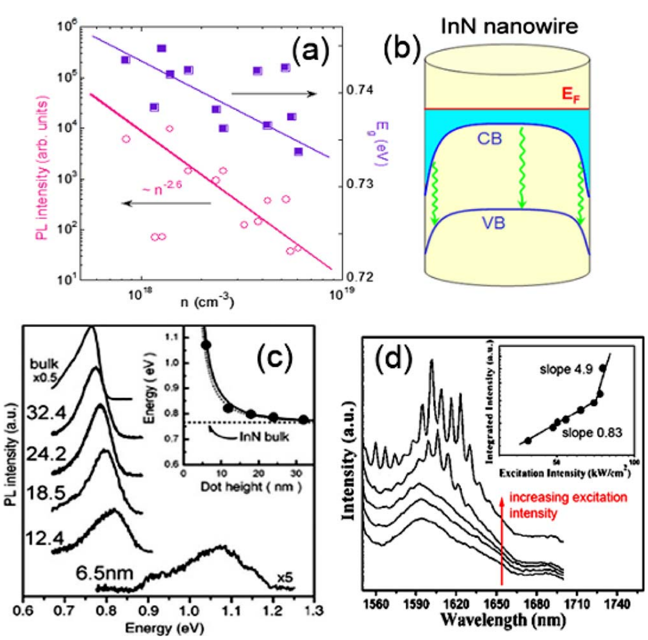

FIG. 35. (Color online) (a) Correlation of electron concentration with the PL integral intensity and bandgap E_g in InN NWs. Reference 266. (b) A schematic band diagram illustrating the electron-hole recombination between the conduction band (CB) and valence band (VB) of an InN NW, where an electron accumulation layer exists on the surface due to surface Fermi level pinning. (c) PL spectra measured at 17 K for InN bulk and InN quantum dots with different heights. The insert shows the peak energy as a function of dot height. The solid line (dotted line) is calculated by effective mass approximation using $0.042m_0$ ($0.07m_0$) as the electron effective mass. Reference 277. (d) Lasing of InN nanobelts at high photoexcitation intensities. The inset shows the emission intensity as a function of excitation intensity. Reference 276.

As in other semiconductor nanostructures, the optical bandgap of InN increases in the presence of substantial quantum confinement. The characteristic length scale for this to become significant is comparable to the exciton Bohr radius, which is on the order of 10 nm for InN. Chao *et al.*[269] reported a blueshift of the PL spectra with decreasing InN nanorod diameters. The PL intensity depends linearly on the excitation power over two orders of magnitude (5–300 mW), indicating the interband transition nature of the luminescence. Similar blueshift in PL has been observed in InN quantum dots as well. Figure 35(c) shows the PL spectra of self-assembled InN QDs embedded in GaN grown by MOCVD.[277] The QD height was measured by AFM, and determines the degree of confinement in the QDs. The peak energies shift systematically from 0.78 to 1.07 eV as the average dot height was reduced from 32.4 to 6.5 nm. The inset shows that the PL peak shift can be well explained by a standard quantum confinement model within the effective mass approximation.[277]

Ultraviolet lasing has been achieved in ZnO nanowires where the facetted surfaces form natural resonance cavities.[280] Similar lasing activities have been observed in InN nanobelts for infrared wavelengths.[275,276] These InN nanobelts were grown by MOCVD along the [110] direction and were enclosed by {001} and $\{1\bar{1}0\}$ planes. As shown in Fig. 35(d), the nanobelts undergo a transition from spontaneous emission to stimulated emission when the excitation power is above a threshold. Sharp lasing peaks emerge on top of the broad spontaneous emission peak, where the lasing wavelengths are determined by the Fabry–Pérot cavity of the nanobelts.

B. InN nanostructures: Electronic properties

Electroluminescence (EL) is a powerful tool to probe the electron-photon interactions in single NWs in the field-effect transistor geometry where the nanowire is electrically biased between a source and a drain electrode. Spectrally resolved light emission is recorded as a function of the biasing voltage and back gate voltage. Chen *et al.* have performed such EL experiments on single InN NWs.[281] The EL spectrum shows a peak near E_g of InN and blueshifts at higher temperature. The EL intensity increases with increasing biasing voltage V_d as $\exp(-V_0/V_d)$, where V_0 is a parameter depending on the optical phonon scattering length in the NW. These observations agree well with an impact excitation mechanism. The surface accumulation layer was found to enhance the radiative electron-hole recombination in these InN nanowires through a plasmon-exciton coupling mechanism.

FETs using InN NWs with diameters between 70 and 150 nm have been fabricated. The electron mobility in these devices was extracted by measuring the transconductance in response to a gate voltage. It was found that the mobility is comparable to bulk InN with similar doping.[282] In similar experiments, the dependence of resistance on the nanowire diameter was found to deviate from simple geometric scaling, and attributed to stronger surface influence.[283,284] Recently, Bloemers *et al.*[285,286] measured the magnetoresistance of single InN nanowires at variable temperatures. Information on phase coherent transport is obtained by analyzing the characteristic fluctuation pattern in the magnetoconductance. The phase coherent length, which defines the nanowire length below which a phase coherent transport is maintained, was determined to be between 200–400 nm depending on temperature. The same group has reported magnetoconductance oscillations with a periodicity corresponding to a single magnetic flux quantum. The effect originates from the phase coherent transport in InN NWs with the unique cylindrical surface conduction geometry.[287]

Other applications of InN nanostructures are also emerging. For example, Wang *et al.* reported excellent field emission properties from InN nanotips.[272] The authors ascribed the superior properties to the intrinsic surface accumulation layer where the band is bent in a manner that the electron tunneling barrier is significantly reduced. Single-walled InN nanotubes were predicted to have the lowest curvature-induced strain energy compared to other group III-V and group IV nanotubes. Calculations show that they are all semiconductors with an almost constant bandgap of about 1 eV.[288]

C. In-rich InGaN nanowires

Nanowire devices harnessing the wide-spectrum possibilities of group-III nitrides have only recently been developed at the laboratory scale. Multicolor LEDs,[257,289–291] lasers,[292] photoelectrodes,[293] and high-mobility FETs (Ref. 294) have been demonstrated with Ga-rich InGaN and GaAlN NWs and NW heterostructures. In these NW devices the highest In content used was 0.35, corresponding to ~600 nm orange-color emission.[289]

Recently Kuykendall *et al.* synthesized $In_xGa_{1-x}N$ NWs utilizing a combinatorial low-temperature halide CVD.[295] X-ray and electron diffraction prove that these NWs were grown as single crystals over the entire composition range of $0<x<1$ across a single substrate with no phase separation. It was argued that these NWs were grown via a self-catalyzed process enabled by the low growth temperature (550 °C) and high growth rate which stabilizes thermodynamically unstable product. Figure 36 shows the optical characterization of these NWs. Despite the strong "yellow luminescence" for Ga-rich compositions which is typical for Ga-rich InGaN thin films as well, these NWs exhibit bandgap values spanning from the infrared (1.2 eV) to the ultraviolet (3.4 eV) spectral range. This range is consistent with the narrow bandgap of InN, and shows great potential for

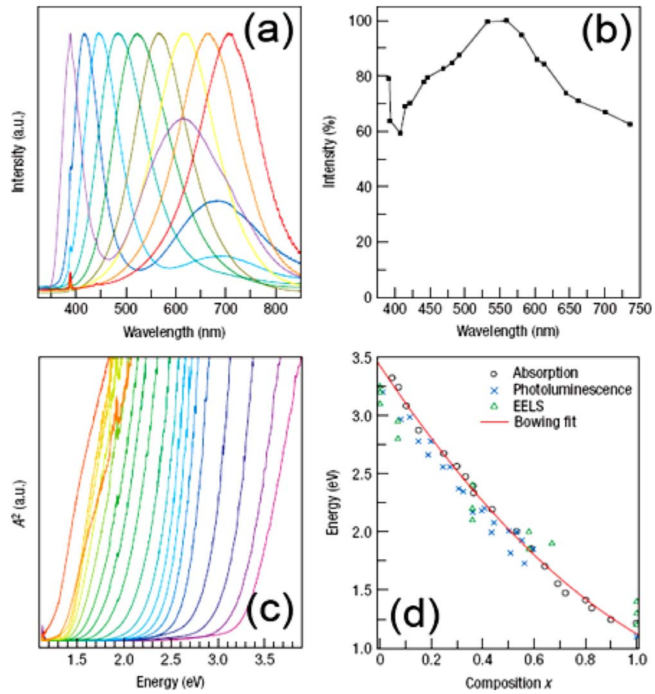

FIG. 36. (Color online) (a) PL emission of $In_xGa_{1-x}N$ NWs ($x=0-0.6$). (b) PL peak intensities as a function of peak wavelength for different compositions. (c) Optical absorption spectra ($x=0-1$). (d) Bandgap plotted as a function of In fraction x for PL, absorption and EELS, and a bowing equation fit to absorption data. Reference 295.

fabricating nanoscale full-color light emitting and light harvesting devices. One of the remarkable properties of these NWs is the high quantum efficiency over a wide range of compositions [Fig. 36(b)], which overcomes the "green valley of death" drop off in PL efficiency for InGaN thin films.[4] The authors suggest that this improvement is due to the unique growth mechanism and geometry of NWs; these help relax strain and eliminate threading dislocations, which usually act as nonradiative recombination centers in InGaN thin films.

VI. CONCLUSIONS AND OUTLOOKS

We have presented an up-to-date review of the physical properties and applications of InN and related group III-nitride alloys.

InN has the largest cation-anion electronegativity difference and atomic mass ratio among all group III-V semiconductors. As a consequence of these unique characteristics InN features an unusually low conduction band minimum and a wide phononic bandgap. Extraordinary materials properties thus arise in InN, including a nonparabolic conduction band, a small electron effective mass, intrinsic surface electron accumulation, strong background electron doping, high radiation resistance, and slowed hot phonon cooling. After the revision of the narrow bandgap of InN, fundamental band parameters of InN and In-rich InGaN and InAlN alloys have been re-evaluated and were summarized in this review.

The bandgaps of group III-nitride alloys continuously span a wide spectrum ranging from the near infrared to the ultraviolet. Significant impact is expected on device applications by the group-III nitrides. Most interestingly, the direct bandgaps of $In_{1-x}Ga_xN$ alloys provide an almost perfect match to the solar spectrum. This opens up an interesting opportunity for using these alloys in high-efficiency, multi-junction solar cells. InN-related group III-nitride alloys may also find applications in the areas of full-color LEDs, lasers, components for 1.55 μm fiber optics, terahertz radiation emitters, high-power, and high-speed transistors, and chemical sensors. Realization of these devices relies on the control of materials quality, surface states, and *p*-type doping, which are currently under intense investigation. Unintentional *n*-type doping in InN is attributed, at least partially, to native defects. *p*-type activity in Mg-doped InN and InGaN has been confirmed by several groups. However, the activation rate of acceptors is currently below 25%.[134,144] A large percentage of the acceptors is compensated by the unintentional donors. Control of surface states remains a major challenge in this field. Passivation of surface states to remove the surface electron accumulation is much desired for probing and contacting the bulk. In the meantime, such a surface electron accumulation layer is exploited for chemical sensing and field-effect devices.

Low temperature is crucial for prevention of phase separation and interfacial diffusion in the growth of InGaN alloys and heterostructures. With the rapid progress in synthesis, doping, and integration, fabrication of InGaN thin film and nanowire devices over the entire composition and spectral range is on the horizon. This will open a wide avenue to a new class of high-efficiency, wide-spectrum, and long-lifetime electronic and optoelectronic devices based on group-III nitrides. We note that a book on studies of InN and related group III-nitride alloys has been edited by Veal, *et al.*[296] Interested readers are referred to this book for more information on the growth, doping, phonon, and electronic properties, band structure, defect physics, microstructures, and low-dimensional structures of these materials.

ACKNOWLEDGMENTS

This review would not have been written without the invitation of Professor J. M. Poate and Professor E. E. Haller. I am grateful to have the opportunity to present recent developments in the research field of InN and In-rich group-III nitrides. I wish to acknowledge collaborations and discussions with Dr. W. Walukiewicz, Dr. H. Lu, Dr. W. J. Schaff, Professor E. E. Haller, Professor Y. Nanishi, Dr. K. M. Yu, Dr. J. W. Ager III, and Dr. S. X. Li. This work was supported, in part, by the National Science Foundation under Grant No. EEC-0425914, and in part by the Laboratory Directed Research and Development Program of Lawrence Berkeley National Laboratory under the Department of Energy Contract No. DE-AC02-05CH11231.

[1]S. Nakamura, J. Vac. Sci. Technol. A **13**, 705 (1995).
[2]S. Nakamura, Science **281**, 956 (1998).
[3]J. M. Phillips, M. E. Coltrin, M. H. Crawford, A. J. Fischer, M. R. Krames, R. Mueller-Mach, G. O. Mueller, Y. Ohno, L. E. S. Rohwer, J. A. Simmons, and J. Y. Tsao, Laser Photonics Rev. **1**, 307 (2007).
[4]D. Fuhrmann, Appl. Phys. Lett. **88**, 071105 (2006).
[5]Basic Research Needs for Solid-State Lighting, Report of the DOE Basic Energy Sciences Workshop on Solid State Lighting, 2006.
[6]H. J. Hovel and J. J. Cuomo, Appl. Phys. Lett. **20**, 71 (1972).
[7]V. A. Tyagi, V. A. Eustigneev, A. M. Krasilo, A. F. Andreeva, and V. Y. Malatidiou, Sov. Phys. Semicond. **11**, 1257 (1977).
[8]K. L. Westra, R. P. W. Lawson, and M. J. Brett, J. Vac. Sci. Technol. A **6**, 1730 (1988).
[9]T. L. Tansley and C. P. Foley, J. Appl. Phys. **59**, 3241 (1986).
[10]H. Morkoc, *Nitride Semiconductors and Devices* (Springer, Heidelberg, 1999).
[11]S. Nakamura and S. F. Chichibu, *Introduction to Nitride Semiconductor Blue Lasers and Light Emitting Diodes* (Taylor & Francis, London, 2000).
[12]S. Yamaguchi, M. Kariya, S. Nitta, T. Takeuchi, C. Wetzel, H. Amano, and I. Akasaki, Appl. Phys. Lett. **76**, 876 (2000).
[13]T. Matsuoka, H. Tanaka, T. Sasaki, and K. Katsui, paper presented at the Proceedings of the 16th International Symposium on GaAs and Related Compounds, Karuizawa, 1989 ; [Inst. Phys. Conf. Ser. **106**, 141 (1990)].
[14]H. Lu, W. J. Schaff, J. Hwang, H. Wu, G. Koley, and L. F. Eastman, Appl. Phys. Lett. **79**, 1489 (2001).
[15]V. Y. Davydov, A. A. Klochikhin, R. P. Seisyan, V. V. Emtsev, S. V. Ivanov, F. Bechstedt, J. Furthmuller, H. Harima, V. Mudryi, J. Aderhold, O. Semchinova, and J. Graul, Phys. Status Solidi B **229**, R1 (2002).
[16]Y. Nanishi, Y. Saito, and T. Yamaguchi, Jpn. J. Appl. Phys., Part 1 **42**, 2549 (2003).
[17]T. Inushima, V. V. Mamutin, V. A. Vekshin, S. V. Ivanov, T. Sakon, M. Motokawa, and S. Ohoya, J. Cryst. Growth **227–228**, 481 (2001).
[18]J. Wu, W. Walukiewicz, K. M. Yu, J. W. Ager, E. E. Haller, H. Lu, W. J. Schaff, Y. Saito, and Y. Nanishi, Appl. Phys. Lett. **80**, 3967 (2002).
[19]T. Matsuoka, H. Okamoto, M. Nakao, H. Harima, and E. Kurimoto, Appl. Phys. Lett. **81**, 1246 (2002).
[20]J. Wu, W. Walukiewicz, W. Shan, K. M. Yu, J. W. Ager, E. E. Haller, H. Lu, and W. J. Schaff, Phys. Rev. B **66**, 201403 (2002).
[21]J. Wu, W. Walukiewicz, W. Shan, K. M. Yu, J. W. Ager, S. X. Li, E. E. Haller, H. Lu, and W. J. Schaff, J. Appl. Phys. **94**, 4457 (2003).
[22]A. G. Bhuiyan, A. Hashimoto, and A. Yamamoto, J. Appl. Phys. **94**, 2779 (2003).
[23]T. Matsuoka, Superlattices Microstruct. **37**, 19 (2005).
[24]Y. Huang, H. Wang, Q. Sun, J. Chen, D. Y. Li, Y. T. Wang, and H. Yang, J. Cryst. Growth **276**, 13 (2005).
[25]A. G. Bhuiyan, K. Sugita, K. Kasashima, A. Hashimoto, A. Yamamoto, and V. Y. Davydov, Appl. Phys. Lett. **83**, 4788 (2003).
[26]A. Yamamoto, T. Tanaka, K. Koide, A. Hashimoto, Phys. Status Solidi A **194**, 510 (2002).
[27]R. S. Q. Fareed, R. Jain, R. Gaska, M. S. Shur, J. Wu, W. Walukiewicz, and M. A. Khan, Appl. Phys. Lett. **84**, 1892 (2004).
[28]V. Cimalla, J. Pezoldt, G. Ecke, R. Kosiba, O. Ambacher, L. Spiess, G. Teichert, H. Lu, and W. J. Schaff, Appl. Phys. Lett. **83**, 3468 (2003).
[29]P. Schley, R. Goldhahn, C. Napierala, G. Gobsch, J. Schoermann, D. J. As, K. Lischka, M. Feneberg, and K. Thonke, Semicond. Sci. Technol. **23**, 055001 (2008).
[30]C. L. Hsiao, T. W. Liu, C. T. Wu, H. C. Hsu, G. M. Hsu, L. C. Chen, W. Y. Shiao, C. C. Yang, A. Gallstrom, P. O. Holtz, C. C. Chen, and K. H. Chen, Appl. Phys. Lett. **92**, 111914 (2008).
[31]J. G. Lozano, F. M. Morales, R. Garcia, D. Gonzalez, V. Lebedev, C. Y. Wang, V. Cimalla, and O. Ambacher, Appl. Phys. Lett. **90**, 091901 (2007).
[32]M. Ueno, M. Yoshida, A. Onodera, O. Shimomura, and K. Takemura, Phys. Rev. B **49**, 14 (1994).
[33]H. Lu, W. J. Schaff, J. Hwang, H. Wu, W. Yeo, A. Pharkya, and L. F. Eastman, Appl. Phys. Lett. **77**, 2548 (2000).
[34]I. Vurgaftman, J. R. Meyer, and L. R. Ram-Mohan, J. Appl. Phys. **89**, 5815 (2001).
[35]M. E. Levinshtein, S. L. Rumyantsev, and M. S. Shur, *Properties of Advanced Semiconductor Materials: GaN, AlN, InN, BN, SiC, SiGe* (Wiley, New York, 2001).
[36]J. C. Phillips, *Bonds and Bands in Semiconductors* (Academic, New York, 1973).
[37]O. Ambacher, M. S. Brandt, R. Dimitrov, T. Metzger, M. Stutzmann, R. A. Fischer, A. Miehr, A. Bergmaier, and G. Dollinger, J. Vac. Sci. Technol. B **14**, 3532 (1996).
[38]T. Inushima, M. Higashiwaki, and T. Matsui, Phys. Rev. B **68**, 235204 (2003).
[39]A. Kasic, M. Schubert, Y. Saito, Y. Nanishi, and G. Wagner, Phys. Rev. B **65**, 115206 (2002).
[40]I. Vurgaftman and J. R. Meyer, J. Appl. Phys. **94**, 3675 (2003).
[41]K. B. Nam, M. L. Nakarmi, J. Li, J. Y. Lin, and H. X. Jiang, Appl. Phys. Lett. **83**, 878 (2003).
[42]N. Khan, N. Nepal, A. Sedhain, J. Y. Lin, and H. X. Jiang, Appl. Phys.

Lett. **91**, 012101 (2007).
[43]R. Goldhahn, P. Schley, A. T. Winzer, G. Gobsch, V. Cimalla, O. Ambacher, M. Rakel, C. Cobet, N. Esser, H. Lu, and W. J. Schaff, Phys. Status Solidi A **203**, 42 (2006).
[44]R. Goldhahn, P. Schley, A. T. Winzer, M. Rakel, C. Cobet, N. Esser, H. Lu, and W. J. Schaff, J. Cryst. Growth **288**, 273 (2006).
[45]P. Schley, R. Goldhahn, A. T. Winzer, G. Gobsch, V. Cimalla, O. Ambacher, H. Lu, W. J. Schaff, M. Kurouchi, Y. Nanishi, M. Rakel, C. Cobet, and N. Esser, Phys. Rev. B **75**, 205204 (2007).
[46]C. Buchheim, R. Goldhahn, M. Rakel, C. Cobet, N. Esser, U. Rossow, D. Fuhrmann, A. Hangleiter, Phys. Status Solidi B **242**, 2610 (2005).
[47]H. Harima, J. Phys.: Condens. Matter **14**, R967 (2002).
[48]V. Y. Davydov, V. V. Emstev, J. N. Goncharuk, A. N. Smimov, V. D. Petrikov, V. V. Mamutin, V. A. Vekshin, S. V. Ivanov, M. B. Smimov, and T. Inushima, Appl. Phys. Lett. **75**, 3297 (1999).
[49]S. P. Fu, Y. F. Chen, and K. W. Tan, Solid State Commun. **137**, 203 (2006).
[50]J. Bhattacharyya, S. Ghosh, M. R. Gokhale, B. M. Arora, H. Lu, and W. J. Schaff, Appl. Phys. Lett. **89**, 151910 (2006).
[51]S. Ghosh, P. Misra, H. T. Grahn, B. Imer, S. Nakamura, S. P. DenBaars, and J. S. Speck, J. Appl. Phys. **98**, 026105 (2005).
[52]G. Shikata, S. Hirano, T. Inoue, M. Orihara, Y. Hijikata, H. Yaguchi, and S. Yoshida, J. Cryst. Growth **301–302**, 517 (2007).
[53]E. O. Kane, J. Phys. Chem. Solids **1**, 249 (1957).
[54]P. Y. Yu and M. Cardona, *Fundamentals of Semiconductors: Physics and Materials Properties* (Springer-Verlag, Berlin, 1999).
[55]P. Rinke, M. Winkelnkemper, A. Qteish, D. Bimberg, J. Neugebauer, and M. Scheffler, Phys. Rev. B **77**, 075202 (2008).
[56]S. P. Fu and Y. F. Chen, Appl. Phys. Lett. **85**, 1523 (2004).
[57]Y. M. Chang, H. W. Chu, C. H. Shen, H. Y. Chen, and S. Gwo, Appl. Phys. Lett. **90**, 072111 (2007).
[58]S. H. Wei and A. Zunger, Phys. Rev. B **60**, 5404 (1999).
[59]N. E. Christensen and I. Gorczyca, Phys. Rev. B **50**, 4397 (1994).
[60]H. Akamaru, A. Onodera, T. Endo, and O. Mishima, J. Phys. Chem. Solids **63**, 887 (2002).
[61]G. Franssen, I. Gorczyca, T. Suski, A. Kaminska, J. Pereiro, E. Munoz, E. Iliopoulos, A. Georgakilas, S. B. Che, Y. Ishitani, A. Yoshikawa, E. Christensen, and A. Svane, J. Appl. Phys. **103**, 033514 (2008).
[62]A. Kaminska, G. Franssen, T. Suski, I. Gorczyca, N. E. Christensen, A. Svane, A. Suchocki, H. Lu, W. J. Schaff, E. Dimakis, and A. Georgakilas, Phys. Rev. B **76**, 075203 (2007).
[63]S. X. Li, J. Wu, E. E. Haller, W. Walukiewicz, W. Shan, H. Lu, and W. J. Schaff, Appl. Phys. Lett. **83**, 4963 (2003).
[64]A. V. Rodina and B. K. Meyer, Phys. Rev. B **64**, 245209 (2001).
[65]J. Wu, W. Walukiewicz, S. X. Li, R. Armitage, J. C. Ho, E. R. Weber, E. E. Haller, H. Lu, W. J. Schaff, A. Barcz, and R. Jakiela, Appl. Phys. Lett. **84**, 2805 (2004).
[66]B. Arnaudov, T. Paskova, P. P. Paskov, B. Magnusson, E. Valcheva, B. Monemar, H. Lu, W. J. Schaff, H. Amano, and I. Akasaki, Phys. Rev. B **69**, 115216 (2004).
[67]J. Wu, W. Walukiewicz, K. M. Yu, W. Shan, J. W. Ager, E. E. Haller, H. Lu, W. J. Schaff, W. K. Metzger, and S. Kurtz, J. Appl. Phys. **94**, 6477 (2003).
[68]T. Inushima, T. Yaguchi, A. Nagase, A. Iso, and T. Shiraishi, Inst. Phys. Conf. Ser. **142**, 197 (1996).
[69]T. Inushima, T. Shiraishi, and V. Y. Davydov, Solid State Commun. **110**, 491 (1999).
[70]T. Hofmann, T. Chavdarov, V. Darakchieva, H. Lu, W. J. Schaff, and M. Schubert, Phys. Status Solidi C **3**, 1854 (2006).
[71]I. Gorczyca, J. Plesiewicz, L. Dmowski, T. Suski, N. E. Christensen, A. Svane, C. S. Gallinat, G. Koblmueller, and J. S. Speck, J. Appl. Phys. **104**, 013704 (2008).
[72]W. Paul and R. V. Jones, Proc. Phys. Soc. B **66**, 194 (1953).
[73]P. D. C. King, T. D. Veal, P. H. Jefferson, S. A. Hatfield, L. F. J. Piper, C. F. McConville, F. Fuchs, J. Furthmüller, F. Bechstedt, H. Lu, and W. J. Schaff, Phys. Rev. B **77**, 045316 (2008).
[74]S. H. Wei, X. Nie, I. G. Batyrev, and S. B. Zhang, Phys. Rev. B **67**, 165209 (2003).
[75]C. Y. Yeh, S. H. Wei, and A. Zunger, Phys. Rev. B **50**, 2715 (1994).
[76]M. V. Schilfgaarde, A. Sher, and A. B. Chen, J. Cryst. Growth **178**, 8 (1997).
[77]T. Kotani and M. V. Schilfgaarde, Solid State Commun. **121**, 461 (2002).
[78]K. A. Johnson and N. W. Ashcroft, Phys. Rev. B **58**, 15548 (1998).
[79]D. Vogel, P. Krueger, and J. Pollmann, Phys. Rev. B **55**, 12836 (1997).
[80]M. Usuda, N. Hamada, K. Shiraishi, and A. Oshiyama, Jpn. J. Appl. Phys., Part 1 **43**, L407 (2004).
[81]P. Carrier and S. H. Wei, Appl. Phys. Lett. **97**, 33707 (2005).
[82]F. Bechstedt and J. Furthmuller, J. Cryst. Growth **246**, 315 (2002).
[83]D. Bagayoko, L. Franklin, and G. L. Zhao, Appl. Phys. Lett. **96**, 4297 (2004).
[84]D. Bagayoko and L. Franklin, J. Appl. Phys. **97**, 123708 (2005).
[85]D. Fritsch, H. Schmidt, and M. Grundmann, Phys. Rev. B **69**, 165204 (2004).
[86]M. Losurdo, G. Bruno, T. H. Kim, S. Choi, and A. Brown, Appl. Phys. Lett. **88**, 121928 (2006).
[87]S. Logothetidis, J. Petalas, M. Cardona, and T. D. Moustakas, Phys. Rev. B **50**, 18017 (1994).
[88]A. Kasic, E. Valcheva, B. Monemar, H. Lu, and W. J. Schaff, Phys. Rev. B **70**, 115217 (2004).
[89]J. Schörmann, D. J. As, K. Lischka, P. Schley, R. Goldhahn, S. F. Li, L. Loeffler, M. Hetterich, and H. Kalt, Appl. Phys. Lett. **89**, 261903 (2006).
[90]F. Chen, A. N. Cartwright, H. Lu, and W. J. Schaff, Phys. Status Solidi A **202**, 768 (2005).
[91]R. Ascazubi, I. Wilke, S. Cho, H. Lu, and W. J. Schaff, Appl. Phys. Lett. **88**, 112111 (2006).
[92]W. Walukiewicz, J. W. Ager, K. M. Yu, Z. Liliental-Weber, J. Wu, S. X. Li, R. E. Jones, and J. D. Denlinger, J. Phys. D: Appl. Phys. **39**, R83 (2006).
[93]F. Chen, A. N. Cartwright, H. Lu, and W. J. Schaff, Appl. Phys. Lett. **83**, 4984 (2003).
[94]W. Terashima, S. B. Che, Y. Ishitani, and A. Toshikawa, Jpn. J. Appl. Phys., Part 2 **45**, L539 (2006).
[95]J. Wu, W. Walukiewicz, K. M. Yu, J. W. Ager, E. E. Haller, H. Lu, and W. J. Schaff, Appl. Phys. Lett. **80**, 4741 (2002).
[96]J. Wu, W. Walukiewicz, K. M. Yu, J. W. Ager, S. X. Li, E. E. Haller, H. Lu, and W. J. Schaff, Solid State Commun. **127**, 411 (2003).
[97]B. Lee and L. W. Wang, J. Appl. Phys. **100**, 093717 (2006).
[98]C. Caetano, L. K. Teles, M. Marques, A. Dal Pino, and L. G. Ferreira, Phys. Rev. B **74**, 045215 (2006).
[99]V. Y. Davydov, A. A. Klochikhin, V. V. Emtsev, D. A. Kurdyukov, S. V. Ivanov, V. A. Vekshin, F. Bechstedt, J. Furthmuller, J. Aderhold, J. Graul, A. V. Mudryi, H. Harima, A. Hashimoto, A. Yamamoto, and E. E. Haller, Phys. Status Solidi B **234**, 787 (2002).
[100]M. Hori, K. Kano, T. Yamaguchi, Y. Saito, T. Araki, Y. Nanishi, N. Teraguchi, A. Suzuki, Phys. Status Solidi B **234**, 750 (2002).
[101]M. Kurouchi, T. Araki, H. Naoi, T. Yamaguchi, A. Suzuki, and Y. Nanishi, Phys. Status Solidi B **241**, 2843 (2004).
[102]B. N. Pantha, R. Dahal, J. Li, J. Y. Lin, and H. X. Jiang, Appl. Phys. Lett. **92**, 042112 (2008).
[103]S. Yamaguchi, R. Izaki, K. T. Yamagiwa, K. Y. Iwamura, and A. Yamamoto, Appl. Phys. Lett. **83**, 5398 (2003).
[104]T. M. Tritt and M. A. Subramanian, MRS Bull. **31**, 188 (2006).
[105]G. Martin, A. Botchkarev, A. Rockett, and H. Morkoc, Appl. Phys. Lett. **68**, 2541 (1996).
[106]S. R. Lee, A. F. Wright, M. H. Crawford, G. A. Petersen, J. Han, and R. M. Biefeld, Appl. Phys. Lett. **74**, 3344 (1999).
[107]P. Lautenschlager, M. Garriga, L. Vina, and M. Cardona, Phys. Rev. B **36**, 4821 (1987).
[108]C. L. Wu, H. M. Lee, C. T. Kuo, S. Gwo, and C. H. Hsu, Appl. Phys. Lett. **91**, 042112 (2007).
[109]C. G. Van de Walle and J. Neugebauer, Appl. Phys. Lett. **70**, 2577 (1997).
[110]S. H. Wei and A. Zunger, Appl. Phys. Lett. **69**, 2719 (1996).
[111]M. B. Nardelli, K. Rapcewicz, and J. Bernholc, Phys. Rev. B **55**, R7323 (1997).
[112]H. Ünlü, Phys. Status Solidi B **223**, 195 (2001).
[113]C. F. Shih, N. C. Chen, P. H. Chang, and K. S. Liu, Jpn. J. Appl. Phys., Part 1 **44**, 7892 (2005).
[114]P. D. C. King, T. D. Veal, C. E. Kendrick, L. R. Bailey, S. M. Durbin, and C. F. McConville, Phys. Rev. B **78**, 033308 (2008).
[115]C. L. Wu, H. M. Lee, C. T. Kuo, C. H. Chen, and S. Gwo, Appl. Phys. Lett. **92**, 162106 (2008).
[116]K. Wang, C. Lian, N. Su, D. Jena, and J. Timler, Appl. Phys. Lett. **91**, 232117 (2007).
[117]C. Stampfl, C. G. Van der Walle, D. Vogel, P. Krueger, and J. Pollmann, Phys. Rev. B **61**, R7846 (2000).
[118]D. W. Jenkins and J. D. Dow, Phys. Rev. B **39**, 3317 (1989).
[119]X. M. Duan and C. Stampfl, Phys. Rev. B **77**, 115207 (2008).
[120]T. L. Tansley and R. J. Egan, Phys. Rev. B **45**, 10942 (1992).
[121]A. Yamamoto, Y. Murakami, K. Koide, M. Adachi, and A. Hashimoto,

Phys. Status Solidi B **228**, 5 (2001).
[122] A. Laakso, J. Oila, A. Kemppinen, K. Saarinen, W. Egger, L. Liszkay, P. Sperr, H. Lu, and W. J. Schaff, J. Cryst. Growth **269**, 41 (2004).
[123] A. Janotti and C. G. Van de Walle, Appl. Phys. Lett. **92**, 032104 (2008).
[124] S. Limpijumnong, C. G. Van der Walle, Phys. Status Solidi B **228**, 303 (2001).
[125] D. C. Look, H. Lu, W. J. Schaff, J. Jasinski, and Z. Liliental-Weber, Appl. Phys. Lett. **80**, 258 (2002).
[126] E. A. Davis, S. F. J. Cox, R. L. Lichti, and C. G. Van der Walle, Appl. Phys. Lett. **82**, 592 (2003).
[127] G. Pettinari, F. Masia, M. Capizzi, A. Polimeni, M. Losurdo, G. Bruno, T. H. Kim, S. Choi, A. Brown, V. Lebedev, V. Cimalla, and O. Ambacher, Phys. Rev. B **77**, 125207 (2008).
[128] S. P. Fu, T. J. Lin, W. S. Su, C. Y. Shieh, Y. F. Chen, C. A. Chang, N. C. Chen, and P. H. Chang, J. Appl. Phys. **99**, 126102 (2006).
[129] C. G. Van de Walle and J. Neugebauer, Nature (London) **423**, 626 (2003).
[130] M. Yoshimoto, H. Yamamoto, W. Huang, H. Harima, J. Saraie, A. Chayahara, and Y. Horino, Appl. Phys. Lett. **83**, 3480 (2003).
[131] H. Wang, D. S. Jiang, L. L. Wang, X. Sun, W. B. Liu, D. G. Zhan, J. J. Zhu, Z. S. Liu, Y. T. Wang, S. M. Zhang, and H. Yang, J. Phys. D: Appl. Phys. **41**, 135403 (2008).
[132] L. F. J. Piper, T. D. Veal, C. F. McConville, H. Lu, and W. J. Schaff, Appl. Phys. Lett. **88**, 252109 (2006).
[133] R. E. Jones, K. M. Yu, S. X. Li, W. Walukiewicz, J. W. Ager, E. E. Haller, H. Lu, and W. J. Schaff, Phys. Rev. Lett. **96**, 125505 (2006).
[134] P. A. Anderson, C. H. Swartz, D. Carder, R. J. Reeves, S. M. Durbin, S. Chandril, and T. H. Myers, Appl. Phys. Lett. **89**, 184104 (2006).
[135] P. D. C. King, T. D. Veal, P. H. Jefferson, C. F. McConville, H. Lu, and W. J. Schaff, Phys. Rev. B **75**, 115312 (2007).
[136] X. Wang, S. B. Che, Y. Ishitani, and A. Yoshikawa, Appl. Phys. Lett. **90**, 201913 (2007).
[137] X. Wang, S. B. Che, Y. Ishitani, and A. Yoshikawa, Appl. Phys. Lett. **92**, 132108 (2008).
[138] X. Wang, S. B. Che, Y. Ishitani, and A. Yoshikawa, Appl. Phys. Lett. **91**, 242111 (2007).
[139] J. W. L. Yim, R. E. Jones, K. M. Yu, J. W. Ager, W. Walukiewicz, W. J. Schaff, and J. Wu, Phys. Rev. B **76**, 041303(R) (2007).
[140] J. W. Ager, N. Miller, R. E. Jones, K. M. Yu, J. Wu, W. J. Schaff, and W. Walukiewicz, Phys. Status Solidi B **245**, 873 (2008).
[141] A. A. Klochikhin, V. Y. Davydov, V. V. Emtsev, A. V. Sakharov, V. A. Kapitonov, B. A. Andreev, H. Lu, and W. J. Schaff, Phys. Rev. B **71**, 195207 (2005).
[142] N. Miller, J. W. Ager, R. E. Jones, H. M. Smith, E. E. Haller, W. Walukiewicz, W. J. Schaff, C. S. Gallinat, G. Koblmueller, and J. S. Speck, paper presented at the International Workshop on Nitride Semiconductor, Montreux, Switzerland, 2008.
[143] T. Miyajima, S. Uemura, Y. Kudo, Y. Kitajima, A. Yamamoto, D. Muto, and Y. Nanishi, Phys. Status Solidi C **5**, 1665 (2008).
[144] C. A. Chang, T. Y. Tang, P. H. Chang, N. C. Chen, and C. T. Liang, Jpn. J. Appl. Phys., Part 1 **46**, 2840 (2007).
[145] W. J. Schaff, X. Chen, D. Hao, K. Matthews, T. Richards, L. F. Eastman, H. Lu, C. J. Cho, and H. Y. Cha, Phys. Status Solidi B **245**, 868 (2008).
[146] W. Walukiewicz, Physica B **302-303**, 123 (2001).
[147] P. D. C. King, T. D. Veal, H. Lu, P. H. Jefferson, S. A. Hatfield, W. J. Schaff, C. F. McConville, Phys. Status Solidi B **245**, 881 (2008).
[148] T. D. Veal, P. H. Jefferson, L. F. J. Piper, C. F. McConville, T. B. Joyce, P. R. Chalker, L. Considine, H. Lu, and W. J. Schaff, Appl. Phys. Lett. **89**, 202110 (2006).
[149] P. D. C. King, T. D. Veal, A. Adikimenakis, H. Lu, L. R. Bailey, E. Iliopoulos, A. Georgakilas, W. J. Schaff, and C. F. McConville, Appl. Phys. Lett. **92**, 172105 (2008).
[150] V. Gopal, E. H. Chen, E. P. Kvam, and J. M. Woodall, J. Electron. Mater. **29**, 1333 (2000).
[151] H. Lu, W. J. Schaff, L. F. Eastman, and C. E. Stutz, Appl. Phys. Lett. **82**, 1736 (2003).
[152] K. A. Rickert, A. B. Ellis, F. J. Himpsel, H. Lu, and W. J. Schaff, Appl. Phys. Lett. **82**, 3254 (2003).
[153] I. Mahboob, T. D. Veal, C. F. McConville, H. Lu, and W. J. Schaff, Phys. Rev. Lett. **92**, 036804 (2004).
[154] I. Mahboob, T. D. Veal, L. F. J. Piper, C. F. McConville, H. Lu, W. J. Schaff, J. Furthmuller, and F. Bechstedt, Phys. Rev. B **69**, 201307 (2004).
[155] J. Tersoff, Phys. Rev. B **32**, 6968 (1985).
[156] H. Lueth, *Surface and Interfaces of Solid Materials* (Springer, Berlin, 1995).
[157] L. Colakerol, T. D. Veal, H. K. Jeong, L. Plucinski, A. DeMasi, T. Learmonth, P. A. Glans, S. Wang, Y. Zhang, L. F. J. Piper, P. H. Jefferson, A. Fedorov, T. C. Chen, T. D. Moustakas, C. F. McConville, and K. E. Smith, Phys. Rev. Lett. **97**, 237601 (2006).
[158] T. D. Veal, L. F. J. Piper, M. R. Phillips, M. H. Zareie, H. Lu, W. J. Schaff, C. F. McConville, Phys. Status Solidi C **203**, 85 (2006).
[159] P. D. C. King, T. D. Veal, and C. F. McConville, Phys. Rev. B **77**, 125305 (2008).
[160] C. G. Van de Walle and D. Segev, J. Appl. Phys. **101**, 081704 (2007).
[161] K. Xu and A. Yoshikawa, Appl. Phys. Lett. **83**, 251 (2003).
[162] P. D. C. King, T. D. Veal, C. F. McConville, F. Fuchs, J. Furthmuller, F. Bechstedt, P. Schley, R. Goldhahn, J. Schoermann, D. J. As, K. Lischka, D. Muto, H. Naoi, Y. Nanishi, H. Lu, and W. J. Schaff, Appl. Phys. Lett. **91**, 092101 (2007).
[163] C. L. Wu, H. M. Lee, C. T. Kuo, C. H. Chen, and S. Gwo, Phys. Rev. Lett. **101**, 106803 (2008).
[164] G. F. Brown, M. A. Mayer, W. J. Schaff, W. Walukiewicz, and J. Wu, Appl. Phys. Lett. **93**, 262105 (2008).
[165] S. R. Messenger, G. P. Summers, E. A. Burke, R. J. Walters, and M. A. Xapsos, Prog. Photovoltaics **9**, 103 (2001).
[166] S. X. Li, K. M. Yu, J. Wu, R. E. Jones, W. Walukiewicz, J. W. Ager, W. Shan, E. E. Haller, H. Lu, and W. J. Schaff, Phys. Rev. B **71**, 161201 (2005).
[167] F. Tuomisto, A. Pelli, K. M. Yu, W. Walukiewicz, and W. J. Schaff, Phys. Rev. B **75**, 193201 (2007).
[168] T. B. Fehlberg, G. A. Umana-Membreno, B. D. Nener, G. Parish, C. S. Gallinat, G. Koblmueller, S. Rajan, S. Bernardis, and J. S. Speck, Jpn. J. Appl. Phys., Part 2 **45**, L1090 (2006).
[169] Z. Yarar, Phys. Status Solidi B **244**, 3711 (2007).
[170] V. M. Polyakov and F. Schwierz, Appl. Phys. Lett. **88**, 032101 (2006).
[171] W. Liang, K. T. Tsen, D. K. Ferry, H. Lu, and W. J. Schaff, Appl. Phys. Lett. **84**, 3681 (2004).
[172] K. T. Tsen, C. Poweleit, D. K. Ferry, H. Lu, and W. J. Schaff, Appl. Phys. Lett. **86**, 222103 (2005).
[173] S. K. O'Leary, B. E. Foutz, M. S. Shur, and L. F. Eastman, J. Mater. Sci.: Mater. Electron. **17**, 87 (2006).
[174] T. Inushima, N. Kato, D. K. Maude, H. Lu, W. J. Schaff, R. Tauk, Y. Meziani, S. Ruffenach, O. Briot, W. Knap, B. Gil, H. Miwa, A. Yamamoto, D. Muto, Y. Nanishi, M. Higashiwaki, T. Matsui, Phys. Status Solidi B **243**, 1679 (2006).
[175] C. T. Liang, Z. H. Sun, C. L. Hsiao, M. Z. Hsu, L. W. Tu, J. Y. Lin, J. H. Chen, Y. F. Chen, and C. T. Wu, Appl. Phys. Lett. **90**, 172101 (2007).
[176] R. E. Jones, S. X. Li, L. Hsu, K. M. Yu, W. Walukiewicz, Z. Liliental-Weber, J. W. Ager, E. E. Haller, H. Lu, and W. J. Schaff, Physica B **376–377**, 436 (2006).
[177] R. E. Jones, H. C. M. Van Genuchten, S. X. Li, L. Hsu, K. M. Yu, W. Walukiewicz, J. W. Ager, E. E. Haller, H. Lu, and W. J. Schaff, Mater. Res. Soc. Symp. Proc. **892**, FF06 (2006).
[178] L. Hsu, R. E. Jones, S. X. Li, K. M. Yu, and W. Walukiewicz, J. Appl. Phys. **102**, 073705 (2007).
[179] X. G. Yu and X. G. Liang, J. Appl. Phys. **103**, 043707 (2008).
[180] W. Shan, W. Walukiewicz, E. E. Haller, B. D. Little, J. J. Song, M. D. McCluskey, N. M. Johnson, Z. C. Feng, M. Schurman, and R. A. Stall, J. Appl. Phys. **84**, 4452 (1998).
[181] P. Perlin, L. Mattos, N. A. Shapiro, J. Kruger, W. S. Wong, T. Sands, N. W. Cheung, and E. R. Weber, J. Appl. Phys. **85**, 2385 (1999).
[182] T. Suski, H. Teisseyre, S. P. Lepkowski, P. Perlin, H. Mariette, T. Kitamura, Y. Ishida, H. Okumura, and S. F. Cichibu, Phys. Status Solidi B **235**, 225 (2003).
[183] L. Bellaiche, K. Kunc, and M. Besson, MRS Internet J. Nitride Semicond. Res. **1**, 1 (1996).
[184] B. Welber, M. Cardona, C. K. Kim, and S. Rodriguez, Phys. Rev. B **12**, 5729 (1975).
[185] S. Adachi, J. Appl. Phys. **58**, R1 (1985).
[186] A. Janotti and C. G. Van de Walle, Phys. Rev. B **75**, 121201 (2007).
[187] H. Schulz and K. H. Thiemann, Solid State Commun. **23**, 815 (1977).
[188] P. Perlin, I. Gorczyca, E. Christensen, I. Grzegory, H. Teisseyre, and T. Suski, Phys. Rev. B **45**, 13307 (1992).
[189] Q. Xia, H. Xia, and A. L. Ruoff, J. Appl. Phys. **73**, 8189 (1993).
[190] T. Mashimo, M. Uchino, A. N. T. Kobayashi, E. Takasawa, T. S. Y. Noguchi, H. Hikosaka, K. Fukuoka, and Y. Syono, J. Appl. Phys. **86**, 6710 (1999).
[191] M. Ueno, A. Onodera, O. Shimomura, and K. Takemura, Phys. Rev. B **45**, 10123 (1992).

[192] M. T. Hasan, A. G. Bhuiyan, and A. Yamamoto, Solid-State Electron. **52**, 134 (2008).
[193] Y. C. Kong, Y. D. Zheng, C. H. Zhou, Y. Z. Deng, B. Shen, S. L. Gu, R. Zhang, P. Han, R. L. Jiang, and Y. Shi, Solid-State Electron. **49**, 199 (2005).
[194] Z. Yarar, B. Ozdemir, and M. Ozdemir, J. Electron. Mater. **36**, 1303 (2007).
[195] V. Y. Davydov, A. A. Klochikhin, M. B. Smirnov, V. V. Emtsev, V. D. Petrikov, I. A. Abroyan, A. I. Titov, J. N. Goncharuk, A. N. Smirnov, V. V. Mamutin, S. V. Ivanov, T. Inushima, Phys. Status Solidi B **216**, 779 (1999).
[196] J. W. Ager, W. Walukiewicz, W. Shan, K. M. Yu, S. X. Li, E. E. Haller, H. Lu, and W. J. Schaff, Phys. Rev. B **72**, 155204 (2005).
[197] S. Hernandez, R. Cusco, D. Pastor, L. Artus, K. P. O'Donnell, R. W. Martin, I. M. Watson, Y. Nanishi, and E. Calleja, J. Appl. Phys. **98**, 013511 (2005).
[198] C. Kittel, *Introduction to Solid State Physics*, 8th ed. (Wiley, New York, 2004).
[199] P. Würfel, Sol. Energy Mater. Sol. Cells **46**, 43 (1997).
[200] P. G. Klemens, Phys. Rev. **148**, 845 (1966).
[201] B. K. Ridley, J. Phys.: Condens. Matter **8**, L511 (1996).
[202] G. J. Conibeer, D. Koenig, M. A. Green, and J. F. Guillemoles, Thin Solid Films **516**, 6948 (2008).
[203] D. Zanato, N. Balkan, B. K. Ridley, G. Hill, and W. J. Schaff, Semicond. Sci. Technol. **19**, 1024 (2004).
[204] V. Pacebutas, G. Aleksejenko, A. Krotkus, J. W. Ager, W. Walukiewicz, H. Lu, and W. J. Schaff, Appl. Phys. Lett. **88**, 191109 (2006).
[205] S. Z. Sun, Y. C. Wen, S. H. Guo, H. M. Lee, S. Gwo, and C. K. Sun, J. Appl. Phys. **103**, 123513 (2008).
[206] Y. C. Wen, C. Y. Chen, C. H. Shen, S. Gwo, and C. K. Sun, Appl. Phys. Lett. **89**, 232114 (2006).
[207] J. W. Pomeroy, M. Kuball, H. Lu, W. J. Schaff, X. Wang, and A. Yoshikawa, Appl. Phys. Lett. **86**, 223501 (2005).
[208] A. Devos, *Endoreversible Thermodynamics of Solar Energy Conversion* (Oxford University Press, New York, 1992).
[209] H. Hamzaoui, A. S. Bouazzi, and B. Rezig, Sol. Energy Mater. Sol. Cells **87**, 595 (2005).
[210] S. R. Kurtz, P. Faine, and J. M. Olson, J. Appl. Phys. **68**, 1890 (1990).
[211] L. Hsu and W. Walukiewicz, J. Appl. Phys. **104**, 024507 (2008).
[212] R. Stevenson, Compound Semicond. **12**, 27 (2006).
[213] A. Barnett *et al.*, paper presented at the 22nd European Photovoltaic Solar Energy Conference, Milan, Italy, 2007.
[214] N. H. Rafat and S. E. D. Habib, Sol. Energy Mater. Sol. Cells **55**, 341 (1998).
[215] N. Miller, R. E. Jones, K. M. Yu, J. W. Ager, Z. Liliental-Weber, E. E. Haller, W. Walukiewicz, T. L. Williamson, and M. A. Hoffbauer, Phys. Status Solidi C **5**, 1866 (2008).
[216] S. Gwo, C. L. Wu, C. H. Shen, W. H. Chang, T. M. Hsu, J. S. Wang, and J. T. Hsu, Appl. Phys. Lett. **84**, 3765 (2004).
[217] C. L. Hsiao, L. W. Tu, M. Chen, Z. W. Jiang, N. W. Fan, Y. J. Tu, and K. R. Wang, Jpn. J. Appl. Phys., Part 2 **44**, L1076 (2005).
[218] J. Grandal and M. A. Sanchez-Garcia, J. Cryst. Growth **278**, 373 (2005).
[219] B. Maleyre, S. Ruffenach, O. Briot, B. Gil, and A. Van der Lee, Superlattices Microstruct. **36**, 517 (2004).
[220] T. Yodo, Y. Kitagawa, K. Miyaki, H. Yona, and Y. Harada, Jpn. J. Appl. Phys., Part 2 **43**, L139 (2004).
[221] T. Yamaguchi, Y. Saito, C. Morioka, K. Yorozu, T. Araki, A. Suzuki, and Y. Nanishi, Phys. Status Solidi B **240**, 429 (2003).
[222] C. L. Wu, C. H. Shen, H. W. Lin, H. M. Lee, and S. Gwo, Appl. Phys. Lett. **87**, 241916 (2005).
[223] M. A. Sanchez-Garcia, J. Grandal, E. Calleja, S. Lazic, J. M. Calleja, A. Trampert, Phys. Status Solidi B **243**, 1490 (2006).
[224] C. H. Shen, H. Y. Chen, H. W. Lin, S. Gwo, A. A. Klochikhin, and V. Y. Davydov, Appl. Phys. Lett. **88**, 253104 (2006).
[225] C. C. Huang, R. W. Chuang, S. J. Chang, J. C. Lin, Y. C. Cheng, and W. J. Lin, J. Electron. Mater. **37**, 1054 (2008).
[226] M. Jamil, R. A. Arif, Y. K. Ee, H. Tong, J. B. Higgins, N. Tansu, Phys. Status Solidi A **205**, 1619 (2008).
[227] Z. Y. Li, S. M. Lan, W. Y. Uen, Y. R. Chen, M. C. Chen, Y. H. Huang, C. T. Ku, S. M. Liao, T. N. Yang, S. C. Wang, and G. C. Chi, J. Vac. Sci. Technol. A **26**, 587 (2008).
[228] C. Yang, X. Wang, H. Xiao, J. Ran, C. Wang, G. Hu, X. Wang, X. Zhang, J. Li, and J. Li, Phys. Status Solidi A **204**, 4288 (2007).
[229] O. Jani, H. Yu, E. Trybus, B. Jampana, I. Ferguson, A. Doolittle, and C. Honsberg, paper presented at the 22nd European Photovoltaic Solar Energy Conference, Milan, Italy, 2007.
[230] X. Chen, K. D. Matthews, D. Hao, W. J. Schaff, L. F. Eastman, Phys. Status Solidi A **205**, 1103 (2008).
[231] C. J. Neufeld, N. G. Toledo, S. C. Cruz, M. Iza, S. P. DenBaars, and U. K. Mishra, Appl. Phys. Lett. **93**, 143502 (2008).
[232] O. Jani, I. Ferguson, C. Honsberg, and S. Kurtz, Appl. Phys. Lett. **91**, 132117 (2007).
[233] P. T. Barletta, E. A. Berkman, B. F. Moody, N. A. El-Masry, A. M. Emara, M. J. Reed, and S. M. Bedair, Appl. Phys. Lett. **90**, 151109 (2007).
[234] T. Xu, A. Y. Nikiforov, R. France, C. Thomidis, A. Williams, and T. D. Moustakas, Phys. Status Solidi A **204**, 2098 (2007).
[235] S. B. Che, T. Mizuno, X. Wang, Y. Ishitani, and A. Yoshikawa, J. Appl. Phys. **102**, 083539 (2007).
[236] I. K. Park, M. K. Kwon, J. O. Kim, S. B. Seo, J. Y. Kim, J. H. Lim, S. J. Park, and Y. S. Kim, Appl. Phys. Lett. **91**, 133105 (2007).
[237] N. K. Van Der Laak, R. A. Oliver, M. J. Kappers, and C. J. Humphreys, Appl. Phys. Lett. **90**, 121911 (2007).
[238] Y. Sun, Y. H. Cho, E. K. Suh, H. J. Lee, R. J. Choi, and Y. B. Hahn, Appl. Phys. Lett. **84**, 49 (2004).
[239] A. Kikuchi, M. Kawai, M. Tada, and K. Kishino, Jpn. J. Appl. Phys., Part 2 **43**, L1524 (2004).
[240] X. H. Wang, H. Q. Jia, L. W. Guo, Z. G. Xing, Y. Wang, X. J. Pei, J. M. Zhou, and H. Chen, Appl. Phys. Lett. **91**, 161912 (2007).
[241] C. B. Soh, W. Liu, J. H. Teng, S. Y. Chow, S. S. Ang, and S. J. Chua, Appl. Phys. Lett. **92**, 261909 (2008).
[242] A. Yoshikawa, S. B. Che, W. Yamaguchi, H. Saito, X. Q. Wang, Y. Ishitani, and E. S. Hwang, Appl. Phys. Lett. **90**, 073101 (2007).
[243] E. Dimakis, A. Y. Nikiforov, C. Thomidis, L. Zhou, D. J. Smith, J. Abell, C. K. Kao, and T. D. Moustakas, Phys. Status Solidi A **205**, 1070 (2008).
[244] R. Ascazubi, I. Wilke, K. Denniston, H. Lu, and W. J. Schaff, Appl. Phys. Lett. **84**, 4810 (2004).
[245] G. Matthaus, V. Cimalla, B. Pradarutti, S. Riehemann, G. Notni, V. Lebedev, O. Ambacher, S. Nolte, and A. Tuennermann, Opt. Commun. **281**, 3776 (2008).
[246] X. Mu, Y. Ding, K. Wang, D. Jena, and Y. B. Zotova, Opt. Lett. **32**, 1423 (2007).
[247] V. M. Polyakov and F. Schwierz, Semicond. Sci. Technol. **22**, 1016 (2007).
[248] H. Ahn, Y. P. Ku, C. H. Chuang, C. L. Pan, H. W. Lin, Y. L. Hong, and S. Gwo, Appl. Phys. Lett. **92**, 102103 (2008).
[249] H. Lu, W. J. Schaff, and L. F. Eastman, J. Appl. Phys. **96**, 3577 (2004).
[250] O. Kryliouk, H. J. Park, H. T. Wang, B. S. Kang, T. J. Anderson, F. Ren, and S. J. Pearton, J. Vac. Sci. Technol. B **23**, 1891 (2005).
[251] C. F. Chen, C. L. Wu, and S. Gwo, Appl. Phys. Lett. **89**, 252109 (2006).
[252] Y. S. Lu, C. C. Huang, J. A. Yeh, C. F. Chen, and S. Gwo, Appl. Phys. Lett. **91**, 202109 (2007).
[253] Y. S. Lu, C. L. Ho, J. A. Yeh, H. W. Lin, and S. Gwo, Appl. Phys. Lett. **92**, 212102 (2008).
[254] Y. S. Lin, S. H. Koa, C. Y. Chan, S. S. Hsu, H. M. Lee, and S. Gwo, Appl. Phys. Lett. **90**, 142111 (2007).
[255] S. Hauguth-Frank, V. Lebedev, H. J. Buechner, G. Jaeger, and O. Ambacher, Phys. Status Solidi C **5**, 2117 (2008).
[256] V. Lebedev, V. M. Polyakov, S. Hauguth-Frank, V. Cimalla, C. Y. Wang, G. Ecke, F. Schwierz, A. Schober, J. G. Lozano, F. M. Morales, D. Gonzalez, and O. Ambacher, J. Appl. Phys. **103**, 073715 (2008).
[257] Y. Li, F. Qian, J. Xiang, and C. M. Lieber, Mater. Today **9**, 18 (2006).
[258] C. Thelander, P. Agarwal, S. Brongersma, J. Eymery, L. F. Feiner, A. Forchel, M. Scheffler, W. Riess, B. J. Ohlsson, U. Gosele, and L. Samuelson, Mater. Today **9**, 28 (2006).
[259] R. Agarwal and C. M. Lieber, Appl. Phys. A: Mater. Sci. Process. **85**, 209 (2006).
[260] E. Calleja, J. Ristic, S. Fernandez-Garrido, L. Ceruffi, M. A. Sanchez-Garcia, J. Grandal, A. Trampert, U. Jahn, G. Sanchez, A. Griol, and B. Sanchez, Phys. Status Solidi B **244**, 2816 (2007).
[261] C. H. Liang, L. C. Chen, J. S. Hwang, K. H. Chen, Y. T. Hung, and Y. F. Chen, Appl. Phys. Lett. **81**, 22 (2002).
[262] S. Luo, W. Zhou, Z. Zhang, L. Liu, X. Dou, J. Wang, X. Zhao, D. Liu, Y. Gao, L. Song, Y. Xiang, J. Zhou, and S. Xie, Small **1**, 1004 (2005).
[263] T. Tang, S. Han, W. Jin, X. Liu, C. Li, D. Zhang, C. Zhou, B. Chen, J. Han, and M. Meyyaappan, J. Mater. Res. **19**, 423 (2004).
[264] M. C. Johnson, C. J. Lee, E. D. Bourret-Courchesne, S. L. Konsek, S. Aloni, W. Q. Han, and A. Zettl, Appl. Phys. Lett. **85**, 5670 (2004).

[265] S. Vaddiraju, A. Mohite, A. Chin, M. Meyyaappan, G. Sumanasekera, B. W. Alphenaar, and M. K. Sunkara, Nano Lett. **5**, 1625 (2005).
[266] T. Stoica, R. J. Meijers, R. Carlarco, T. Richter, E. Sutter, and H. Luth, Nano Lett. **6**, 1541 (2006).
[267] B. Schwenzer, L. Loeffler, R. Seshadri, S. Keller, F. F. Lange, S. P. DenBaars, and U. K. Mishra, J. Mater. Chem. **14**, 637 (2004).
[268] K. Sardar, F. L. Deepak, A. Govindaraj, M. M. Seikh, and C. N. R. Rao, Small **1**, 91 (2005).
[269] C. K. Chao, H. S. Chang, T. M. Hsu, C. N. Hsiao, C. C. Kei, S. Y. Kuo, and J. I. Chyi, Nanotechnology **17**, 3930 (2006).
[270] Z. H. Lan, W. M. Wang, C. L. Sun, S. C. Shi, C. W. Hsu, T. T. Chen, K. H. Chen, C. C. Chen, Y. F. Chen, and L. C. Chen, J. Cryst. Growth **269**, 87 (2004).
[271] C. Denker, J. Malindretos, F. Werner, F. Limbach, H. Schuhmann, T. Niermann, M. Seibt, and A. Rizzi, Phys. Status Solidi C **5**, 1706 (2008).
[272] K. R. Wang, S. J. Lin, L. W. Tu, M. Chen, Q. Y. Chen, T. H. Chen, M. L. Chen, H. W. Seo, N. H. Tai, S. C. Chang, I. Lo, D. P. Wang, and W. K. Chu, Appl. Phys. Lett. **92**, 123105 (2008).
[273] S. C. Shi, C. F. Chen, G. M. Hsu, J. S. Hwang, T. Chattopadhyay, Z. H. Lan, and L. C. Chen, Appl. Phys. Lett. **87**, 203103 (2005).
[274] L. W. Yin, Y. Bando, D. Golberg, and M. S. Li, Adv. Mater. (Weinheim, Ger.) **16**, 1833 (2004).
[275] M. S. Hu, W. M. Wang, T. T. Chen, L. S. Hong, C. W. Chen, C. C. Chen, Y. F. Chen, K. H. Chen, and L. C. Chen, Adv. Funct. Mater. **16**, 537 (2006).
[276] M. S. Hu, G. M. Hsu, K. H. Chen, C. J. Yu, Y. C. Hsu, L. C. Chen, J. S. Hwang, L. S. Hong, and Y. F. Chen, Appl. Phys. Lett. **90**, 123109 (2007).
[277] W. C. Ke, C. P. Fu, C. Y. Chen, L. Lee, C. S. Ku, W. C. Chou, W. H. Chang, M. C. Lee, W. K. Chen, W. J. Lin, and Y. C. Cheng, Appl. Phys. Lett. **88**, 191913 (2006).
[278] Y. J. Bai, Z. G. Liu, X. G. Xu, D. L. Cui, X. P. Hao, X. Feng, and Q. L. Wang, J. Cryst. Growth **241**, 189 (2002).
[279] S. Ruffenach, O. Briot, M. Moret, and B. Gil, Appl. Phys. Lett. **90**, 153102 (2007).
[280] M. H. Huang, S. Mao, H. Feick, H. Yan, Y. Wu, H. Kind, E. Weber, R. Russo, and P. Yang, Science **292**, 1897 (2001).
[281] J. Chen, G. Cheng, E. Stern, M. A. Reed, and P. Avouris, Nano Lett. **7**, 2276 (2007).
[282] G. Cheng, E. Stern, D. Turner-Evans, and M. A. Reed, Appl. Phys. Lett. **87**, 253103 (2005).
[283] C. Y. Chang, G. C. Chi, W. M. Wang, L. C. Chen, K. H. Chen, F. Ren, and S. J. Pearton, J. Electron. Mater. **35**, 738 (2006).
[284] E. Calleja, J. Grandal, M. A. Sanchez-Garcia, M. Niebelschutz, V. Cimalla, and O. Ambacher, Appl. Phys. Lett. **90**, 262110 (2007).
[285] C. Blömers, T. Schaepers, T. Richter, R. Calarco, H. Lueth, and M. Marso, Phys. Rev. B **77**, 201301 (2008).
[286] C. Blömers, T. Schaepers, T. Richter, R. Calarco, H. Lueth, and M. Marso, Appl. Phys. Lett. **92**, 132101 (2008).
[287] T. Richter, C. Bloemers, H. Lueth, R. Calarco, M. Indlekofer, M. Marso, and T. Schaepers, Nano Lett. **8**, 2834 (2008).
[288] Z. Qian, S. Hou, J. Zhang, R. Li, Z. Shen, X. Zhao, and Z. Xue, Physica E **30**, 81 (2005).
[289] F. Qian, S. Gradecak, Y. Li, C. Wen, and C. M. Lieber, Nano Lett. **5**, 2287 (2005).
[290] H. M. Kim, Y. H. Cho, H. Lee, S. I. Kim, S. R. Ryu, D. Y. Kim, T. W. Kang, and K. S. Chung, Nano Lett. **4**, 1059 (2004).
[291] F. Qian, Y. Li, S. Gradecak, D. Wang, C. J. Barrelet, and C. M. Lieber, Nano Lett. **4**, 1975 (2004).
[292] F. Qian, Y. Li, S. Gradecak, H. G. Park, Y. Dong, Y. Ding, Z. L. Wang, and C. M. Lieber, Nature Mater. **7**, 701 (2008).
[293] W. Luo, B. Liu, Z. Li, Z. Xie, D. Chen, Z. Zou, and R. Zhang, Appl. Phys. Lett. **92**, 262110 (2008).
[294] Y. Li, J. Xiang, F. Qian, S. Gradecak, Y. Wu, H. Yan, D. A. Blom, and C. M. Lieber, Nano Lett. **6**, 1468 (2006).
[295] T. Kuykendall, P. Ulrich, S. Aloni, and P. Yang, Nature Mater. **6**, 951 (2007).
[296] T. D. Veal, C. F. McConville, and W. J. Schaff, *Indium Nitride and Related Alloys* (CRS Press/Taylor & Francis, London, 2009).